

Journal of Geophysical Research: Space Physics

RESEARCH ARTICLE

10.1029/2017JA024852

Key Points:

- Response of Venus magnetosphere to an ICME has been studied by data analysis and hybrid model simulations
- Atypically large magnetic barrier (>250 nT) and magnetization of the ionosphere were observed
- Simulation resulted in a relatively nominal magnetic field draping pattern and about 30% increase of O^+ escape in the ICME run

Correspondence to:

A. P. Dimmock,
andrew.dimmock@irfu.se

Citation:

Dimmock, A. P., Alho, M., Kallio, E., Pope, S. A., Zhang, T. L., Kilpua, E., et al. (2018). The response of the Venusian plasma environment to the passage of an ICME: Hybrid simulation results and Venus Express observations. *Journal of Geophysical Research: Space Physics*, 123. <https://doi.org/10.1029/2017JA024852>

Received 4 OCT 2017

Accepted 1 APR 2018

Accepted article online 6 APR 2018

The Response of the Venusian Plasma Environment to the Passage of an ICME: Hybrid Simulation Results and Venus Express Observations

A. P. Dimmock^{1,2} , M. Alho¹, E. Kallio¹ , S. A. Pope³ , T. L. Zhang^{4,5} , E. Kilpua⁶, T. I. Pulkkinen¹ , Y. Futaana⁷, and A. J. Coates⁸ 

¹Department of Electronics and Nanoengineering, School of Electrical Engineering, Aalto University, Espoo, Finland,

²Swedish Institute of Space Physics, Uppsala, Sweden, ³Department of Automatic Control and Systems Engineering, University of Sheffield, Sheffield, UK, ⁴Harbin Institute of Technology, Shenzhen, China, ⁵Space Research Institute, Austrian Academy of Sciences, Graz, Austria, ⁶Department of Physics, University of Helsinki, Helsinki, Finland, ⁷Swedish Institute of Space Physics, Kiruna, Sweden, ⁸Mullard Space Science Laboratory, University College London, London, UK

Abstract Owing to the heritage of previous missions such as the Pioneer Venus Orbiter and Venus Express, the typical global plasma environment of Venus is relatively well understood. On the other hand, this is not true for more extreme driving conditions such as during passages of interplanetary coronal mass ejections (ICMEs). One of the outstanding questions is how do ICMEs, either the ejecta or sheath portions, impact (1) the Venusian magnetic topology and (2) escape rates of planetary ions? One of the main issues encountered when addressing these problems is the difficulty of inferring global dynamics from single spacecraft orbits; this is where the benefits of simulations become apparent. In the present study, we present a detailed case study of an ICME interaction with Venus on 5 November 2011 in which the magnetic barrier reached over 250 nT. We use both Venus Express observations and hybrid simulation runs to study the impact on the field draping pattern and the escape rates of planetary O^+ ions. The simulation showed that the magnetic field line draping pattern around Venus during the ICME is similar to that during typical solar wind conditions and that O^+ ion escape rates are increased by approximately 30% due to the ICME. Moreover, the atypically large magnetic barrier appears to manifest from a number of factors such as the flux pileup, dayside compression, and the driving time from the ICME ejecta.

1. Introduction

Venus lacks any significant intrinsic magnetic field (Phillips & Russell, 1987). For that reason, the Venus-solar wind (SW) interaction generates an induced magnetosphere (IM) from the interaction between the highly conducting ionosphere and the incoming SW flow. Nevertheless, and remarkably so, the IM contains many similar boundaries and regions to those observed at intrinsic magnetospheres such as the case at Earth.

The global plasma environment of Venus and its magnetic topology during typical solar wind conditions are relatively well understood. Like Earth, a bow shock forms upstream (but stands off only around 1.5 Venus radii, R_v), which is followed by a magnetosheath region downstream housing the shocked solar wind plasma. Forming inside the dayside magnetosheath is the magnetic barrier, which can be identified by the dominance of the magnetic pressure above all other pressure contributions (e.g., thermal and dynamic; Russell et al., 1979). It is the magnetic barrier, as opposed to an intrinsic planetary magnetic field, that acts as an obstacle to the incoming solar wind flow (Zhang et al., 1991). The magnetic barrier ends where the magnetic pressure forms an equilibrium with the upstream solar wind dynamic pressure, and a magnetopause layer forms at the outer edge (Zhang et al., 2007). The Venus IM lies behind the magnetopause and extends to the ionopause, marking the boundary to the Venus ionosphere (Zhang, Delva, et al., 2008). In general, the dayside IM is referred to as the magnetic barrier, whereas the nightside is called the magnetotail. In the present paper, we refer to the IM as the region between the magnetopause and ionopause.

Another crucial aspect of the Venus-SW interaction is the acceleration, pickup, and escape of planetary ions such as O^+ . Heavy ion escape was reported by Mihalov and Barnes (1982), which were inferred from Pioneer Venus Orbiter (PVO) data. Although the identification of O^+ from PVO data was achieved indirectly, it was

proposed that the distribution of O^+ is dictated by the SW convective electric field. This work has been furthered by Venus Express (VEX) observations (Barabash, Fedorov, et al., 2007) confirming that the convective electric field is the controlling parameter, and O^+ escape occurs primarily in the plasma sheet—although pickup can also occur in the magnetosheath. Nevertheless, it is crucial to obtain true ion escape rates to understand the dryness and oxidation of the Venus atmosphere, as well as the time history of water on Venus. However, understanding the global effects on Venus's plasma environment and ion escape during more extreme SW conditions is still an open area of study. An example of such events is interplanetary coronal mass ejection (ICME) which contains, among other features, atypically high upstream dynamic pressures and enhanced solar wind convective electric fields. Another motivation for this is that since ICMEs were speculated to be stronger and more frequent during more active solar periods (Wood et al., 2005), these events may have had a significant impact on Venus's atmosphere and water.

ICMEs are separated into two distinct regions. By this, we refer to the sheath and ejecta regions since their formation as well as field and plasma properties are clearly separate (e.g., Kilpua et al., 2013). ICME sheath regions are easily identified by their compressed and turbulent properties since they often contain high dynamic and thermal pressures, and their magnetic field directions have large-amplitude and irregular fluctuations. The most turbulent parts of the sheath are downstream from a leading shock and upstream of the ejecta leading edge. In contrast, the ejecta exhibits a magnetic field profile which is smooth and slowly varying. They have typically much lower dynamic and thermal pressure than the preceding sheath. Here we focus on the former, when Venus's IM was driven by an ICME sheath for over 3 hr. Such intervals can have dramatic impacts on the Venus environment due to the high upstream dynamic pressures (Edberg et al., 2011; Russell, 1991) and thermalized particles.

Russell and Zhang (1992) and Zhang, Pope, et al. (2008) observed extremely distant bow shock crossings during Venus ICME encounters. The large upstream magnetic field strengths intrinsic to ICMEs can result in magnetosonic Mach numbers approaching unity, if the flow speed remains sufficiently low. As a result, atypically distant bow shock crossings have been observed. For example, Zhang, Pope, et al. (2008) reported a case where the Venus bow shock was crossed at $12 R_V$; scaled to the Earth's magnetosphere, this equates to $180 R_E$. However, it should be noted that these have been observed during the ICME ejecta when the dynamic pressure can be very low. The shocks observed by Zhang, Pope, et al. (2008) and studied in detail by Balikhin et al. (2008) were a new type of shock, driven by pure kinematic relaxation.

Recently, a statistical study on the impact of ICMEs on the position of the Venusian bow shock and magnetic barrier was performed by Vech et al. (2015). The authors reported that the upper and lower boundaries of the magnetic barrier were unaffected by the ICMEs. They also concluded that atypically large magnetic barrier crossings were the result of piled up magnetic field and not a manifestation of compression induced by a change in altitude of the magnetic barrier. The position of the dayside ionosphere was relatively constant, whereas the nightside ionospheric position decreased; they suggested that this is consistent with enhanced ion loss from large dynamic pressures.

What is also noteworthy is that enhanced convective ($\mathbf{E} = -\mathbf{U}_e \times \mathbf{B}$) electric fields (where \mathbf{U}_e is the bulk speed of electrons and \mathbf{B} is the magnetic field) during ICME intervals can accelerate and “pickup” ions leading to their escape (Luhmann et al., 2008). In fact, the interaction between Venus and the SW is one of the only mechanisms in which heavy atmospheric elements can reach the required escape speeds (Luhmann et al., 2008) of ~ 11 km/s (Luhmann & Kozyra, 1991). We should also stress that speeds must be outwardly directed (i.e., not to return to the exobase) for ion escape to be realized. This latter point demonstrates one of the pitfalls of making global interpretations from limited in situ data. It is also important to remember that this effect can also be increased by the reduction of the ionopause altitude, thus exposing a larger area of the upper atmosphere to the solar wind (Luhmann & Cravens, 1991).

The escape of O^+ was investigated by Luhmann et al. (2006) and Luhmann et al. (2007) using PVO observations. In their data, they reported that O^+ fluxes were enhanced by $\sim 100\times$ following large upstream dynamic pressure events such as ICMEs. However, the global interpretations from this study were limited by orbital coverage and short-lived extremes.

Luhmann et al. (2008) continued their work on O^+ escape during ICMEs in a synergistic study using VEX measurements and magnetohydrodynamic test particle simulations. The authors reiterated the point that due to the dynamic nature of the spatial distribution of escaping fluxes, the interpretation reached from in situ mea-

surements can be subjective based on when and where they are sampled—motivating the use of a modeling element in their study. The rotation of the planetary wake induced by interplanetary magnetic field (IMF) rotations can also add to this difficulty. One of the main results from this study was that for certain IMF clock angles, the model suggested that no pickup ions were present along the spacecraft trajectory even though the global pickup ion population in the model and data were identical. The authors concluded that they were only able to conclusively report enhanced escape of O^+ in one case.

Jarvinen et al. (2009) performed a comparative study between VEX observations and hybrid simulation runs. By comparing model and observed data, they could clearly and accurately identify numerous regions (bow shocks, magnetic barrier, central tail current sheet, magnetic tail lobes, magnetosheath, and the planetary wake), indicating that the model achieved consistent results with the data. The escape rates of O^+ were also computed in this study, and the authors reported that the best model-data fit was achieved when O^+ escape rates were between $3 \times 10^{24} \text{ s}^{-1}$ and $1.5 \times 10^{25} \text{ s}^{-1}$. We should also mention that their runs were computed ion escape for nominal solar wind conditions. These rates are consistent with previously reported values between 10^{24} and 10^{26} s^{-1} (Barabash, Fedorov, et al., 2007; Moore et al., 1991).

In the present paper, we investigate the impact on the Venus plasma environment during the passage of a ICME on 5 November 2011 using both observations and kinetic hybrid model results. For the model runs and model-data comparisons, we focus explicitly on the effect from conditions in the sheath region and not the ejecta. On this day, VEX crossed the Venus bow shock after being driven by the ICME sheath region for over 3 hr. The motivation for this study is the 250-nT magnetic barrier which to our knowledge is the largest ever observed; it is the direct result of the ICME passage since typical barrier strengths are 30–40 nT. We also investigate the factors which lead to such a remarkable magnetic field strength. The timeliness of the orbital coverage with respect to the event occurrence also present a rare opportunity to study the effects from the ICME sheath component. We utilize both VEX observations and hybrid simulation results to investigate the global response, which is not possible from the observations alone. High-resolution data are also examined to analyze the waves and turbulence present at the bow shock and in the magnetosheath. In addition, from the simulations, we determine the O^+ escape rate and compare this value to that calculated during ambient conditions and existing values found in the literature.

2. Experimental Data And Model Description

2.1. VEX Data

The present study utilizes observations made by the VEX (Svedhem et al., 2007) spacecraft between 4 and 6 November 2011 in which an ICME passed by the planet. The magnetic field measurements were recorded by the VEX MAGnetometer (Zhang et al., 2006; VEX MAG) at a resolution of 1 and 32 Hz. Since no magnetic cleanliness program was implemented prior to launch, the VEX MAG instrument measures a superposition of ambient and spacecraft generated magnetic fields. An extensive data cleaning program (Pope et al., 2011) was implemented to produce a “cleaned” data set composed only of natural fields which is used here. A magnetic offset correction was also required (Leinweber et al., 2008) prior to a transformation from the VEX spacecraft orientated frame to the Venus Solar Orbital (VSO) coordinate system. Comparable to the Geocentric Solar Ecliptic frame, the VSO system has an x axis orientated toward the Sun, z axis positive north and perpendicular to the orbital plane, and a y axis completing the orthogonal set. In addition to VEX MAG data, we also employ plasma measurements from the Analyzer of Space Plasma and Energetic Atoms (ASPERA-4) instrument (Barabash, Sauvaud, et al., 2007) for the calculation of derived plasma properties and to obtain initial conditions for the simulation runs.

2.2. Hybrid Model Description

The adopted model has been continuously developed for over 15 years to study the response of weakly and nonmagnetized bodies to SW plasma properties. The model has been applied to study the plasma environments of Mercury (Kallio & Janhunen, 2003), Venus (Kallio et al., 2008), the Moon (Kallio, 2005), and Mars (Kallio, Fedorov, et al., 2006). It is a quasi-neutral hybrid particle-in-cell model, and therefore, ions are treated as particles, moving in self-consistently calculated electromagnetic fields. Electrons act as a charge-neutralizing massless fluid, that is,

$$\sum_i q_i n_i + q_e n_e = 0, \quad (1)$$

where (q_e, n_e) , and (q_i, n_i) are the charge and number density of electrons and ions, respectively. The ions in the model move under the Lorentz force $\mathbf{F}_E = q(\mathbf{E} + \mathbf{U}_e \times \mathbf{B})$ where the magnetic field \mathbf{B} is propagated in time from the electric field using Faraday's law,

$$\frac{d\mathbf{B}}{dt} = -\nabla \times \mathbf{E}. \quad (2)$$

The electric field is derived from the electron fluid momentum equation:

$$\mathbf{E} = -\mathbf{U}_e \times \mathbf{B} + \eta \mathbf{J} + \frac{\nabla p_e}{q_e n_e}. \quad (3)$$

Here \mathbf{U}_e is the electron bulk velocity, η the electrical resistivity, and p_e the electron thermal pressure at constant temperature T_e ($p_e = n_e k_B T_e$). Note that the electric current is derived from Ampère's law in which the displacement current has been neglected (i.e., no electromagnetic radiation is included). The magnetic field is then advanced forward in time with a leapfrog algorithm by using equation (2) while particles are accelerated by the Lorentz force. Note that divergence-free condition on the magnetic field is automatically ensured by a Yee lattice grid structure where the magnetic field is assigned to cell faces. Because of the hybrid approach, finite ion gyromotion effects and Hall effects arise naturally. Grid refinement techniques can be used to resolve specific area of the object's environment with a higher precision (see Kallio & Janhunen, 2003, for more thorough technical details), although no refinements were employed in this study. We refer the reader to Jarvinen et al. (2013) for a complete description of the implementation of the model for the Venusian plasma environment. With the exception of the solar wind parameters, the model setup is identical to the one in Jarvinen et al. (2013).

The simulation contains two sources of both planetary O⁺ and H⁺ ions: (i) photoionization of exospheric neutrals as an extended source and (ii) emission of ionospheric ions through the model exobase. The planetary ion production model is identical to the one used by Kallio, Jarvinen, et al. (2006) and later by Jarvinen et al. (2013). Namely, the exospheric cold H⁺ and hot O⁺ sources are separately modeled using the Chamberlain exosphere model with a solar zenith (SZA) dependency, the hot H⁺ corona by an exponential function of the form $n(r) = e^{a_1 r + a_2 + a_3/r}$, with the a_i having a SZ angle dependency (see Kallio, Jarvinen, et al., 2006 for details), and the cold O⁺ as emission of ions from the exobase. These photon processes were the only sources of planetary ions employed.

The simulation does not include a self-consistent ionosphere, and therefore, O⁺ ions originating from the ionosphere are considered by emitting O⁺ ions through the model exobase (see Jarvinen et al., 2013, for details). The O⁺ emission from the model exobase was 1.0×10^{25} 1/s, and the O⁺ photoionization rate was 4.09×10^{24} 1/s, similar to our previous study (Jarvinen et al., 2013). In each analyzed run, the total O⁺ ion production rate (exobase emission + photoionization) was kept constant at 1.4090×10^{25} 1/s. Solar wind and planetary ions which hit the inner obstacle of the model (which represents the exobase) are removed from the simulation. From a physical point of view, this mimics the absorption of ions into the neutral atmosphere. It should be noted that in reality, O⁺ ions are formed also by electron impact ionization and charge exchange and not only by photoionization. However, in the simulation, only photoionization was used in order to compare the previous runs by Jarvinen et al. (2013) and the new runs analyzed in this paper. The reason for this is that all simulations contain identical ion production and, consequently, that all differences between analyzed simulations were attributed purely to different solar wind plasma and field conditions. Finally, when the morphology of the magnetic field is analyzed, it is important to note that the model exobase is the inner obstacle in the simulation, below which the electrical resistivity is set to zero. Therefore, in the simulation, Venus is a superconducting ball inside which magnetic field cannot diffuse. A physical implication from this is that magnetic field lines may "slip" fast around the object. This treatment of the ionosphere may result in an underestimation of the total magnetic field and impact the morphology of the magnetotail and draping pattern.

3. VEX Observations

Presented in Figures 1 and 2 are observations by the VEX magnetometer and ASPERA-4 instruments over multiple time intervals surrounding the passage of the ICME. At around 03:40 UT on 5 November 2011, an ICME shock was detected. This was identified from the leading shock edge clearly visible from the sharp increase in the magnetic field gradient followed by an overall increase in the magnetic field strength downstream, as

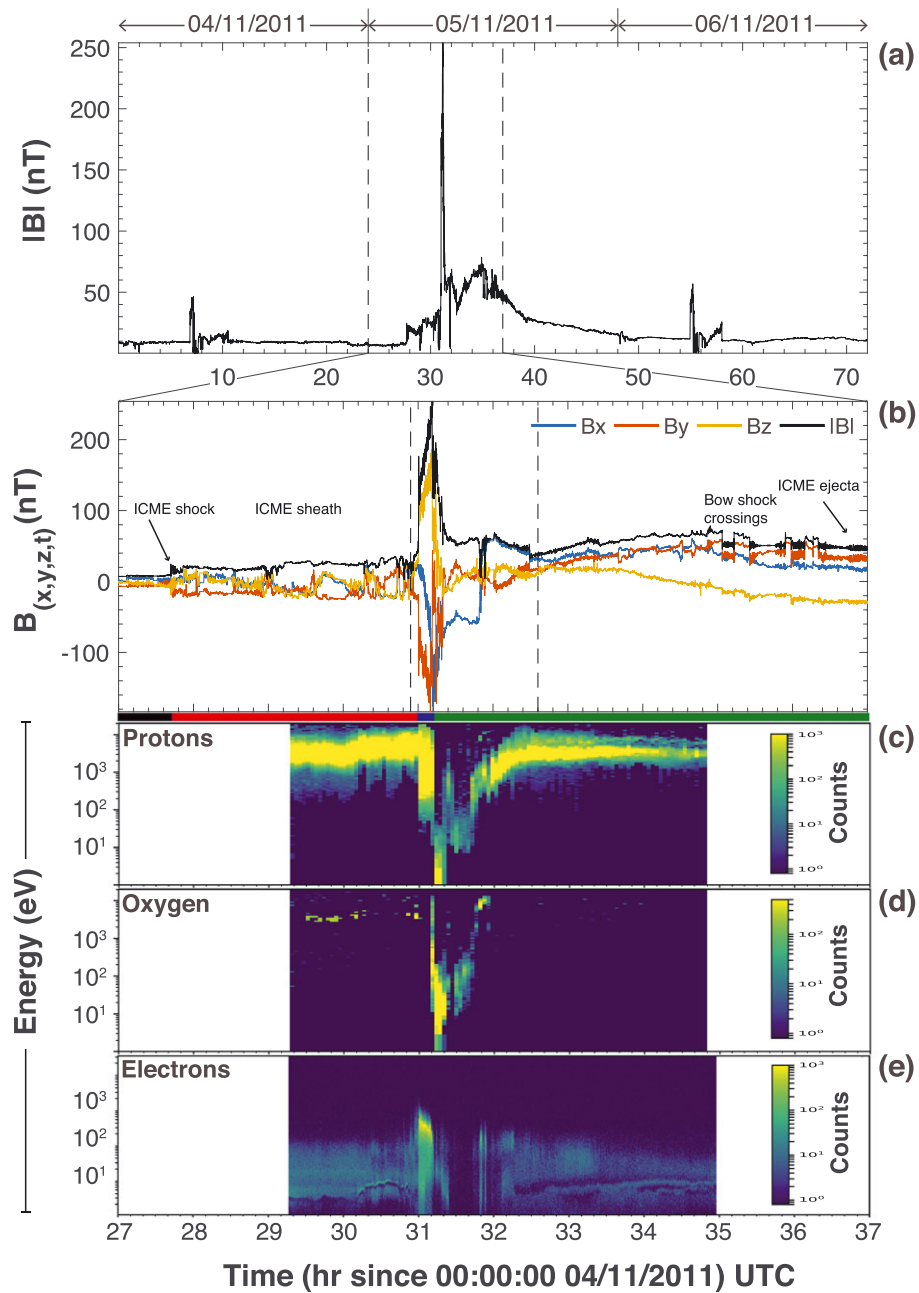


Figure 1. Overview plot of VEX MAG and ASPERA-4 data between 4 and 6 November 2011. Panel (a) shows the VEX MAG data for the entire 3-day interval. Panels (b–e) show the VEX MAG and ASPERA-4 data for 03:00–13:00 5 November 2011 during the passage of the ICME. The colored bars on the horizontal axes correspond to the regions of the orbital path plotted in Figure 3 later. VEX MAG = Venus Express MAGnetometer; ASPERA = Analyzer of Space Plasma and Energetic Atoms; VEX = Venus Express; ICME = interplanetary coronal mass ejection.

shown in Figure 1a. The enhanced field occurred in concert with elevated turbulence and large field rotations which are indicative of an ICME sheath region (Kilpua et al., 2013). Several hours later and clearly shown in Figure 1b, VEX encountered the planetary bow shock at 07:00 UT. This is evident from the dramatic increase of the magnetic field gradient typically associated with a quasi-perpendicular shock front. The actual shock geometry was estimated to be $\theta_{bn} = 58.8^\circ$ by computing the angle between the shock surface normal, $\hat{n} = [0.99, 0.07, 0.12]$, and the average upstream magnetic field, $\mathbf{B}_{up} = [19.06, -22.62, 26.17]$ nT. We estimated the bow shock compression ratio from $B_{cr} = |\mathbf{B}_{up}|/|\mathbf{B}_{down}| = 3.44$, where \mathbf{B}_{down} is the downstream magnetic field; this is compared to 2.9 on the previous day. Although the upstream flow speed is high, the Alfvén Mach

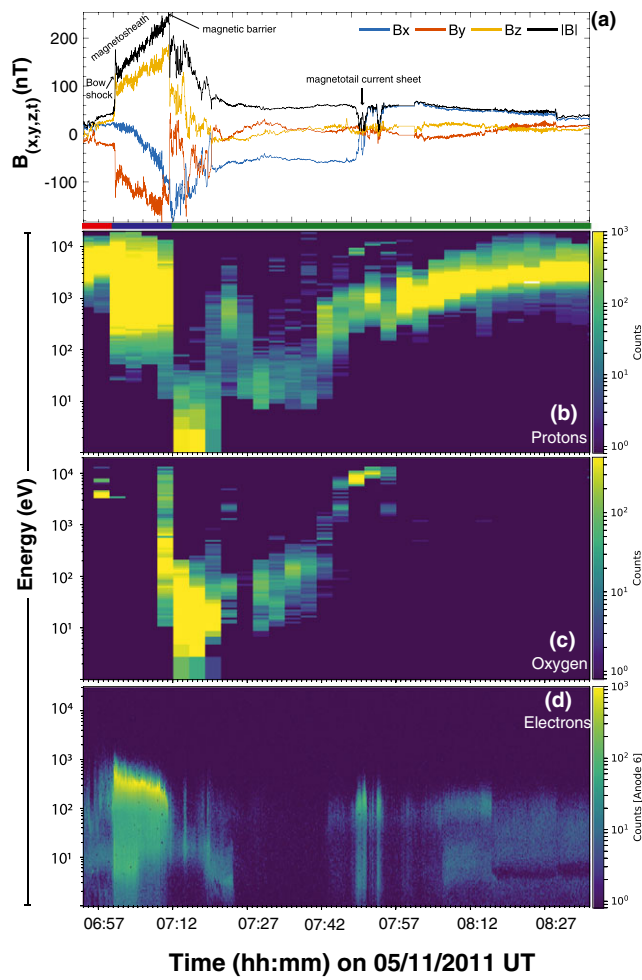


Figure 2. Same format as Figures 1b–1e but for the shorter time interval of 06:54:00–8:36:00 5 November 2011.

number was moderate at $M_A = 3.5$ and therefore explains why no distant bow shock crossings (Zhang, Pope, et al., 2008) occurred on this day. Since the behavior of the magnetic field profile between the ICME shock and the bow shock is consistent, it is our interpretation that VEX occupied the ICME sheath region until reaching the planetary bow shock.

Figures 1c–1e and 2b–2d show the particle data near Venus from the ASPERA-4 ions and electron sensors. The enhanced energy (~ 3 keV) of the solar wind protons upstream of the bow shock is consistent with the heated ICME sheath plasma. According to the ASPERA-4 particle instruments, the properties of the ICME sheath were $\mathbf{U}_i = [-820, -200, -300] \text{ km/s}$, $n_i = 12 \text{ cm}^{-3}$, and $T_i = 60 \text{ eV}$, which were averages computed immediately upstream of the bow shock. One can see in Figure 1c how the solar wind protons are heated and slowed down at the same time in the bow shock where the magnetic field is increased. The slowest protons can be identified near the planet where the magnetic field is at its maximum. The energy of protons starts to increase on the nightside when VEX moves farther from the planet back into the magnetosheath and the solar wind.

The electron data in Figure 1e is also supportive of the identification of these regions and boundaries described above. The low-energy electron population observed in the upstream region is indicative of a more positive spacecraft potential. This beam-like feature is sometimes seen in the electron data and is likely the result of differential charging (Coates et al., 2008). The higher-energy electrons could be either the electron foreshock or associated with the dynamics of the ICME since a change in magnetic field orientation occurs just prior to this at the beginning of the interval.

Interpretation of the oxygen ion data is complicated by the fact that protons can “leak” from the Ion Mass Analyzer (IMA) proton channel into the IMA heavy ion channel, making it difficult to ambiguously determine

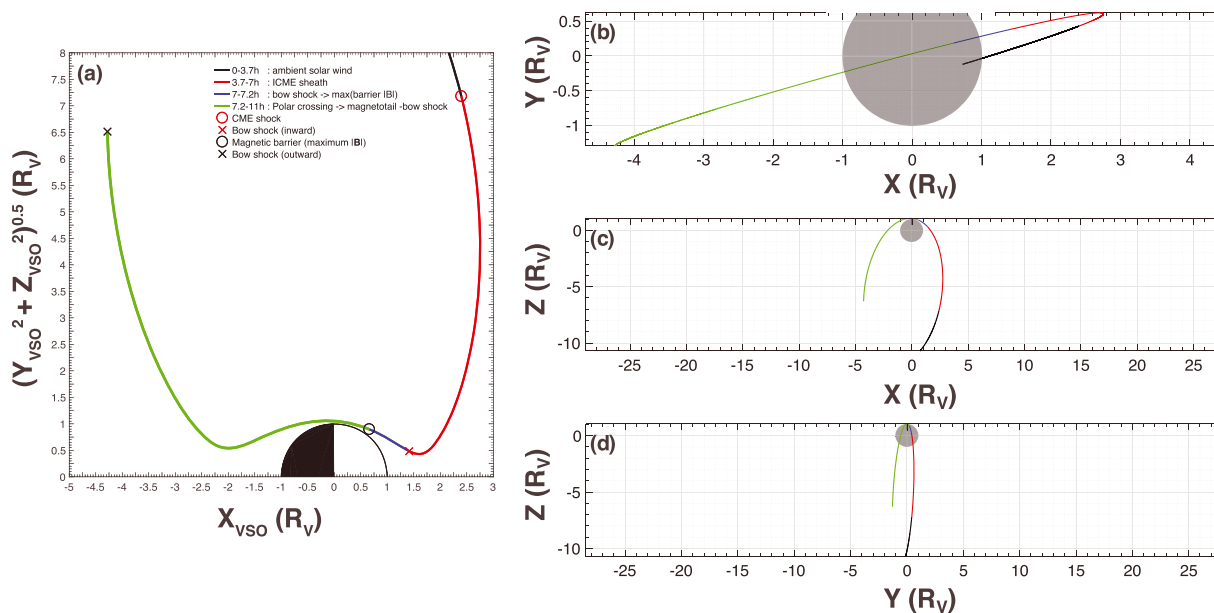


Figure 3. Orbit of VEX on 5 November 2011 in cylindrical coordinates \hat{x} and $\sqrt{\hat{y}^2 + \hat{z}^2}$ (a) and xy , xz , and yz planes (b, c, d), respectively. The color of the line indicates specific intervals during the orbital period and the markers show the crossing of important boundaries. The VEX MAG data for these regions are shown and labeled in Figure 1. VEX = Venus Express; VEX MAG = VEX MAGnetometer; ICME = interplanetary coronal mass ejection.

the relative contribution of oxygen ions and protons in the IMA heavy ion data. For example, the high count rate seen in the heavy ion data in the solar wind at the same energy as where high solar wind proton counts were observed suggests that these heavy ion counts are contaminated with solar wind protons. A clear and high signal of planetary heavy ions can, instead, be seen in Figure 2c at $\sim 07:15$ near the pericenter. The energy of planetary ions increased when VEX moved deeper into the Venusian tail and in the magnetosheath.

Figure 2 shows the magnetic field and particle data near the pericenter more clearly. One can identify high-energy O^+ ions at $\sim 07:25$ and again at $\sim 07:50$. At $\sim 07:50$ and $\sim 07:53$, the magnetic field x component changes direction and there are heated electrons, suggesting that VEX crossed the cross-tail current sheet and the plasma sheet. Although these planetary ions can also be considered to have been “picked up” by the solar wind, their orbits more likely resemble a beam as opposed to the classical cycloid behavior of pickup O^+ ions in the sense that their energy spectrum is rather narrow.

We should note that ICME sheath properties can change significantly when VEX was near Venus. However, such changes cannot be determined once VEX crosses into the downstream region. For example, in Figure 2, one can recognize a sudden appearance of high-energy protons and planetary ions at $\sim 07:25$. This would appear as if VEX had entered for a moment back to the magnetosheath, which may suggest temporal changes in the position of the magnetic barrier and the ionosphere below it. Moreover, there are also decreases of the total magnetic field and increase of the negative magnetic field x component at $\sim 07:18$ and $\sim 07:20$ —similar to the data later at $\sim 07:50$ and $\sim 07:53$. This may indicate that the IMF and, consecutively, the magnetic field draping pattern have varied during the flyby. Thus, any effects from the lack of an upstream monitor are excluded from our analysis, which may manifest as differences between the model-data comparisons we perform later.

Figure 3 provides an overview of the spacecraft orbit on 5 November 2011 from 00:00:00 (solar wind) until leaving the Venus magnetotail into the ICME ejecta. The ejecta is identified from the smooth field rotation (Burlaga et al., 1981) which is in large contrast to the ICME sheath. Interestingly, on closer inspection, the outbound bow shocks from approximately 35 hr in Figure 1a are kinematic relaxation shocks (Balikhin et al., 2008; Zhang, Pope, et al., 2008); this is noteworthy since such shocks are seldom observed, and although beyond the scope of the current study, the conditions leading to their occurrence is worthy of further investigation. The orbital path is presented in a cylindrical coordinate plane in Figure 1a such that the two axes correspond to x and $\sqrt{\hat{y}^2 + \hat{z}^2}$. The xy , xz , and yz are plotted in Figures 1b–1d. Notable time intervals (in hours) have been labeled to mark regions and boundaries of interest. These are (0–3) solar wind, (3–7) ICME sheath,

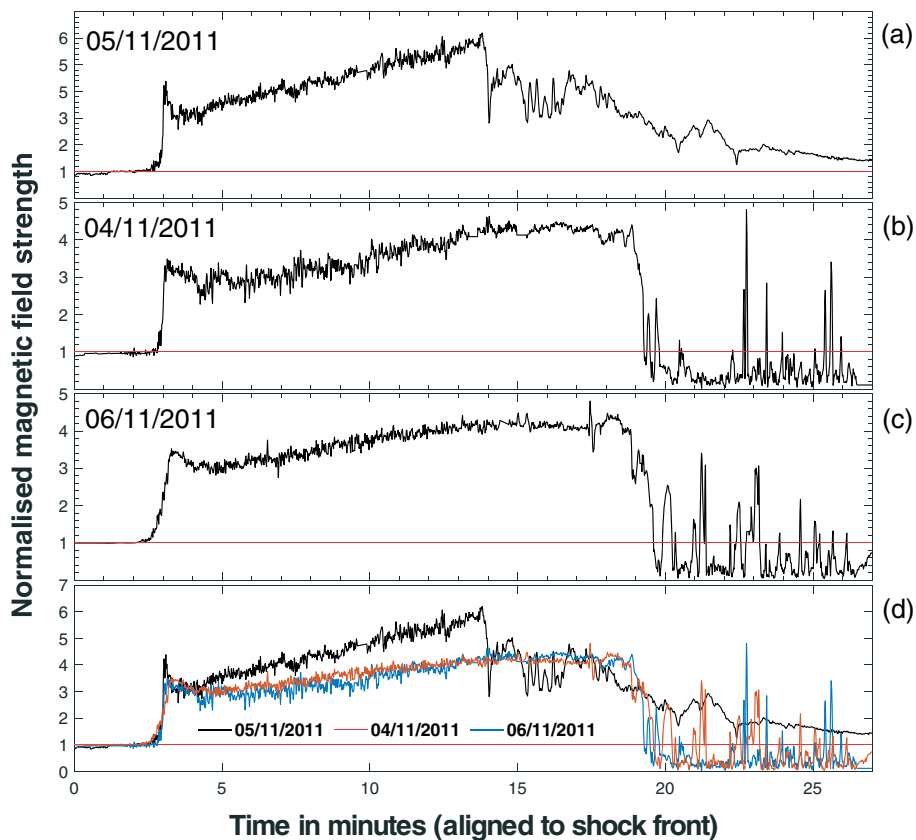


Figure 4. Selected intervals of VEX MAG data on 5 November 2011 (a), 4 November 2011 (b), and 6 November 2011 (c). The top panel is during the ICME encounter and shows larger dayside compression due to the much shorter traversal of the magnetosheath. The relative magnetic field strengths are significantly enhanced during the ICME. The interval following the magnetic barrier in panel (a) is in stark contrast to the other panels, suggesting the ICME driving influences the ionosphere and the ionopause boundary. The horizontal red line marks the value 1 for reference. Panel (d) shows each interval overlaid for comparison and clearly demonstrates the differences in normalized strength and differing nature of the magnetic field after the barrier crossing. VEX MAG = VEX MAGnetometer; ICME = interplanetary coronal mass ejection.

(7–7.2) magnetosheath-magnetic barrier, and (7.2–11) magnetic barrier-magnetotail-outward bow shocks. These regions have also been marked in Figures 1b and 1c by the matching colored horizontal bars. VEX is in a highly polar orbit but crosses the bow shock on the equatorial nose, which is consistent with the estimate of the bow shock normal that points toward the Venus-Sun line. The spacecraft then moves toward the polar region, but before this, the VEX MAG instrument measures an outer edge magnetic barrier strength approximately 250 nT. To our knowledge, this is the largest magnetic barrier strength recorded by VEX. For reference, according to Figure 1a, this is over four times the typical value (~ 50 nT) for similar orbital geometries, as demonstrated by the data measured on 4 and 6 November 2011. In general, the magnetic pressure at the magnetic barrier should balance the upstream dynamic pressure along the barrier normal (Zhang et al., 1991). In the cases of ICME sheath driving, however, there can be a significant thermal upstream pressure from the shocked solar wind plasma. Therefore, it is likely that the simple (dynamic) pressure balance can be violated. In addition, the three-dimensional nature of the magnetic barrier region may prevent the application of a simple one-dimensional pressure balance equation for the ICME interaction.

3.1. Magnetic Barrier and Ionosphere

Figure 4 shows a plot of the magnetic field modulus for three different Venus passages. Figure 4a corresponds to 5 November 2011 which is presented in Figure 2. The remaining intervals are on the surrounding days when the orbital track is similar. The magnetic field measurements have been normalized by the field strength immediately upstream of the bow shock. There are several interesting observations to note from Figure 4. First, the compression ratio ($B_{\text{up}}/B_{\text{down}}$) of the bow shock is larger during the ICME passage, resulting in a larger

downstream magnetic field strength. However, this is not in itself enough to explain such a large magnetic barrier. Second, visually comparing the three panels clearly shows that the magnetosheath traversal is notably shorter in Figure 4a. This could be indicative of an additional compression on the dayside and is also consistent with the fact that the magnetic field gradient as VEX traverses the magnetosheath is much greater. If we are to compute the relative increase of the magnetic field from downstream of the bow shock to the peak of the barrier strength, then the ICME ratio is approximately 1.9 compared to 1.4 and 1.3 on the pristine-driven days. When VEX reaches the magnetic barrier, it is almost six times greater than the upstream field strength compared to approximately four in the other examples. This could also be an indication of enhanced flux pileup, contributing to the magnetic barrier strength. Finally, the magnetic field profile following the magnetic barrier crossing is very different in Figure 4a and does not exhibit the similar sudden drops in magnetic field strength to less than the upstream value in panels Figures 4b and 4c. It is worth noting that in Figure 4a the magnetic field strength remains above its upstream value (red line) even though the spacecraft has crossed significantly into the nightside. The bow shock distance was closer on 5 November 2011 by around $0.2 R_v$, but the magnetic barrier location (based on maximum field strength and subsequent drop) was relatively unchanged—hence the shorter magnetosheath traversal. We direct the readers to the recent paper by Vech et al. (2015) for a comprehensive study on the evolution of the boundary locations.

3.2. The 32-Hz VEXMAG Observations

The smaller-scale features of this event should be investigated since they can provide valuable insight into the presence of pickup ions, energy conversion/dispersion, and also provide evidence of how the local and global plasma conditions are regulated. For that reason, presented in Figure 5 is an interval of high-resolution (32 Hz) measurements made by the VEX MAG instrument over a 220-s interval starting from 06:58:15 UT on 5 November 2011. The data correspond to a traversal by VEX from upstream (ICME sheath) to downstream—the ICME sheath to the Venus magnetosheath. Plotted in Figure 5a is the magnetic field modulus whereas the x , y , and z components are displayed in Figure 5b below. A wavelet spectrogram of $|\mathbf{B}|$ is included in Figure 5c, showing the spectral properties up to 4 Hz. Figures 5d–5i show hodograms of the downstream and upstream waves over approximately two wave cycles. The purple and green vertical lines in Figure 5a mark the instance that these were computed. What is immediately obvious from Figure 5c is the increase in amplitude of fluctuations above 1 Hz from approximately 20 s. The upstream region (20–100 s) shows higher-frequency (>1 Hz) waves which extend far into the upstream region. There are also waves housed in the bow shock foot region which are of similar frequency but higher amplitude. Downstream of the bow shock from 130 s, there are large-amplitude ($B_{\text{RMS}}/B_0 \sim 0.2$) waves which persist for approximately 80 s. The signature of these waves appeared to be damped soon after this interval. The hodograms from both upstream and downstream suggest that the wave packets are almost circularly polarized ($\lambda_{\text{int}}/\lambda_{\text{max}} \sim 1$) and (where λ are the eigenvalues of the covariance matrix) propagate obliquely at an angle of 34° (upstream) and 35° (downstream) with respect to the average background field direction. The frequency of the upstream (downstream) waves is approximately 4.5 Hz (1.2 Hz) which compared to the local proton gyrofrequency of 0.6 Hz (1.95 Hz). There are a number of candidates for these waves such as whistler waves (Russell, 2007), ion cyclotron waves (Delva et al., 2008; Wei et al., 2011), and nonlinear magnetic structures (Walker et al., 2011). It is our interpretation that the waves upstream are Doppler-shifted whistler mode waves as similar dispersive wave trains are commonly observed upstream of planetary bow shocks (Dimmock et al., 2013) with comparable characteristics. We also suggest that the downstream waves are also likely whistler waves transmitted from upstream. We also investigated the possibility that the downstream waves were ion cyclotron waves, however, although this analysis proved inconclusive as they appeared to propagate obliquely to the background field direction. Nevertheless, we have not eliminated this possibility since (1) both wave modes can exist here, (2) it is difficult to confirm a wave mode with one spacecraft, and (3) some properties (e.g., frequency) of the structures are consistent with multiple wave modes.

4. VEX and Hybrid Simulation Comparison

For a global perspective, we utilize hybrid simulations for the ICME interval. For the ICME sheath input conditions, we made two runs: one with the measured density (n_{12}) of 12 cm^{-3} and another with a significantly increased upstream density of 20 cm^{-3} (n_{20}). We also made an additional run for nominal upstream conditions to compare with the ICME runs. The list of model input parameters for the three runs can be found in Table 1. The reason for making these two runs was to determine the impact from the upstream density (and

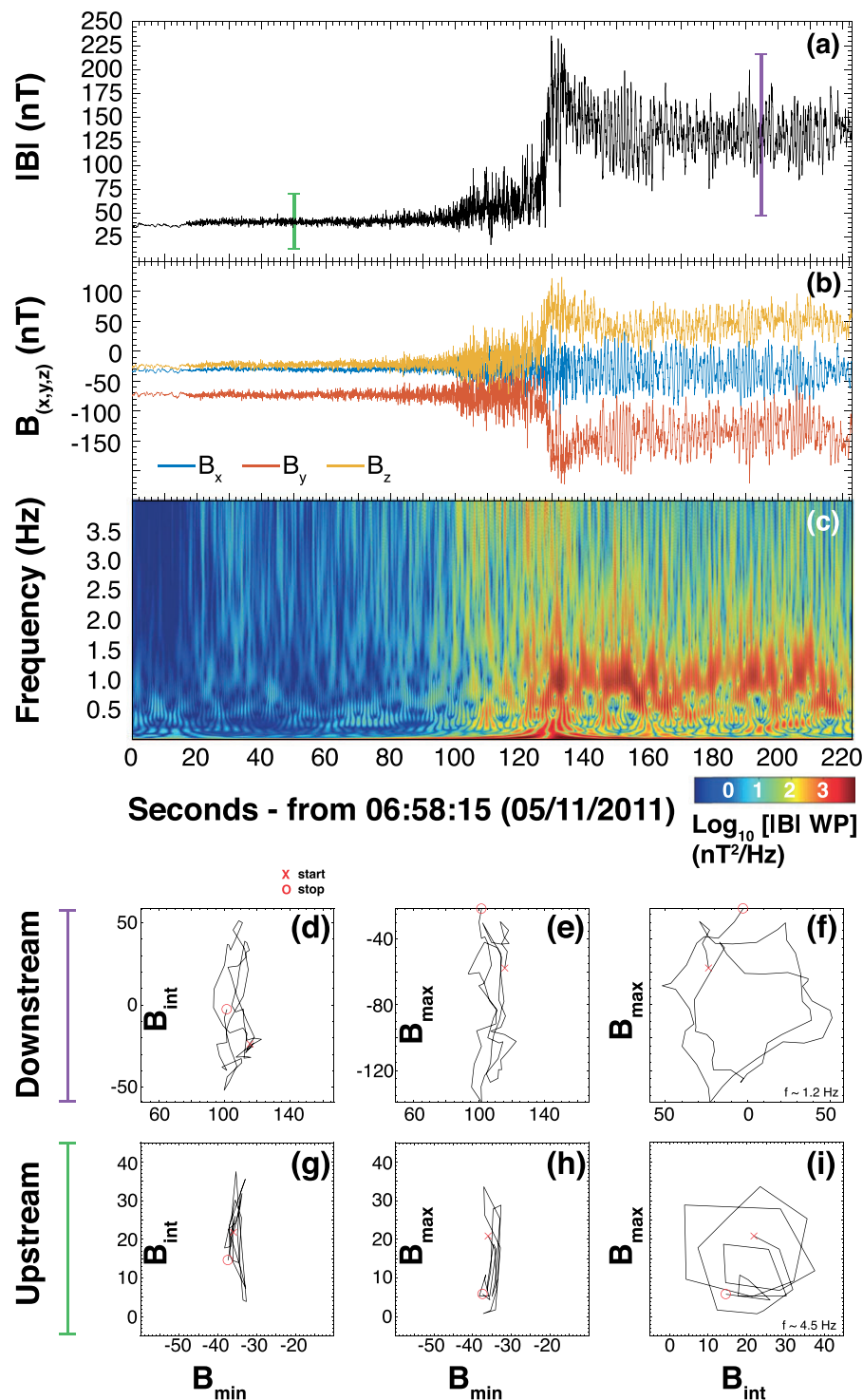


Figure 5. VEX MAG measurements recorded at 32 Hz. The interval demonstrates the spacecraft crossing from the upstream (ICME sheath) to the downstream Venus magnetosheath. The entire interval shown here was during the time that the ICME sheath was passing Venus. Panel (a) shows $|B|$ whereas the x , y , and z components are plotted below in panel (b). A wavelet spectrogram of $|B|$ is plotted in panel (c), and the color scale corresponds to the Log_{10} of the wavelet power. It is clearly shown from panel (c) that there are well-defined wave packets both upstream and downstream of the bow shock at multiple frequencies. Hodograms from minimum variance analysis of the upstream and downstream wave packets are included in panels (d–i) and suggest near-circular polarization for both cases. In these panels, subscripts min, int, and max correspond to the magnetic field along the minimum, intermediate, and maximum variance directions. VEX MAG = VEX MAGnetometer ICME = interplanetary coronal mass ejection.

Table 1
Input Parameters to the Kinetic Hybrid Simulations for the Three Runs Used in this Study

Parameter	Nominal	ICME n_{12}	ICME n_{20}
dx (km); R_V	302.59; 0.05	302.59; 0.05	302.59; 0.05
dt (s)	0.02	0.01	0.01
Domain extents (km); R_V	$\pm 18, 155.4 (\pm 3)$	$\pm 18, 155.4 (\pm 3)$	$\pm 18, 155.4 (\pm 3)$
Inner boundary (exobase) radius (km)	6,251.8	6,251.8	6,251.8
Macroparticles per cell	30	30	30
Solar wind IMF, $ \mathbf{IMF} $ (nT)	[6, -5, 0], 7.81	[20, -20, 20], 34.64	[20, -20, 20], 34.64
Solar wind bulk velocity (km/s)	[-400, 0, 0]	[-800, -200, -300]	[-800, -200, -300]
Solar wind proton density (cm^{-3})	8	12	20
Solar wind proton temperature (K)	116,045	696,270	696,270
Isothermal electron temperature (K)	10,000	10,000	10,000

subsequent external pressure) on the model result. This is an important question since the density can be large and often underestimated during extreme upstream conditions. The primary goals for the model-data comparison and model-data analysis were to (1) determine if the model could approach the strength of the magnetic barrier with atypically larger upstream densities, (2) determine the impact on the O^+ escape rates for different upstream densities, and (3) study the differences between the model and experimental magnetic topology during such extreme driving conditions. For comparative purposes, a run for nominal conditions was also generated ($\mathbf{B} = [6.0, -5.0, 0.0]$ nT, $n_i = 8 \text{ cm}^{-3}$, $U = [-400, 0, 0]$ km/s). In this section, we compare the observations with the model solutions. As an error metric, we compare the field line draping in the model to the one measured by VEX. We exploit a feature of the model to attempt to optimize the angle between the model and the measurement, in effect, “mimicking” a variation in the upstream clock angle.

The simulation is set up with cylindrical symmetry in all parameters describing the planet, except for IMF clock angle. Thus, the results of a single simulation can be transformed by a rotation about the x axis to match a different IMF clock angle, when the solar wind is flowing along the x direction. Therefore, a single run can be used to analyze the set of given upstream parameters, the IMF clock angle taking any value and all other parameters held constant. When applied to dynamic variations in the solar wind, we need to assume, additionally, that changes in solar wind are slower than the response times of the system and that there are no hysteresis effects. Both assumptions may be violated in reality, but we still regard the method as a useful approximation. This is utilized when comparing the VEX observations with the hybrid model results, since any rotation about the x axis of the simulation domain can account for unknown clock angle variations.

For each VEX orbital point, we identify the corresponding hybrid model grid. We then trace a circular path in the yz plane with radius $|\mathbf{R}_{\text{vex}}|$ with an angular resolution of 1° . This is equivalent to rotating the hybrid model box at 1° increments, which adjusts the model solution for changes in the IMF clock angle. From this point, we denote this angle as Θ , and $\Delta\Theta$ is the angular displacement from the beginning of the circular path. At each point on the circular path, \mathbf{B}_{hyb} is interpolated and a rotation about the axis of $-\Delta\Theta$ is applied ($\mathbf{B}_{\text{hyb}}^*$). From this point, subscripts of hyb refer to simulated parameters. The angle between \mathbf{B}_{vex} and $\mathbf{B}_{\text{hyb}}^*$ is measured and recorded (θ_o). This procedure is repeated for each VEX orbital point which falls in the hybrid model simulation domain, and points outside the simulation model limits are excluded. The optimal orbital point is selected based on the minimum value of θ_o at each location. Prior to this procedure, \mathbf{B}_{vex} is smoothed by a 60-point moving average filter. The purpose of this is to decrease the impact from small-scale temporal and spatial magnetic field variations which are not included in the hybrid model.

4.1. Optimization for ICME Day: 5 November 2011

Presented in Figure 6 is a comparison of \mathbf{B}_{vex} and $\mathbf{B}_{\text{hyb}}^*$ for the data collected on 5 November 2011. Here we show data from the n_{20} ICME run in which the upstream density was 20 cm^{-3} . The simulated points were selected based on the minimization of θ_o . Figures 6a–6c show each component in which subscripts 1 and 2 (e.g., $a_{1,2}$) correspond to the actual values and those normalized by the root mean square (RMS), respectively—computed over the entire interval. Figure 6d corresponds to Θ , and is the angle of VEX, in the yz plane. Any changes in Θ , can be interpreted as variations in the IMF clock angle. The units of the x axis are given in both data points and UT time according to the VEX measurement. For reference, the bow shock is

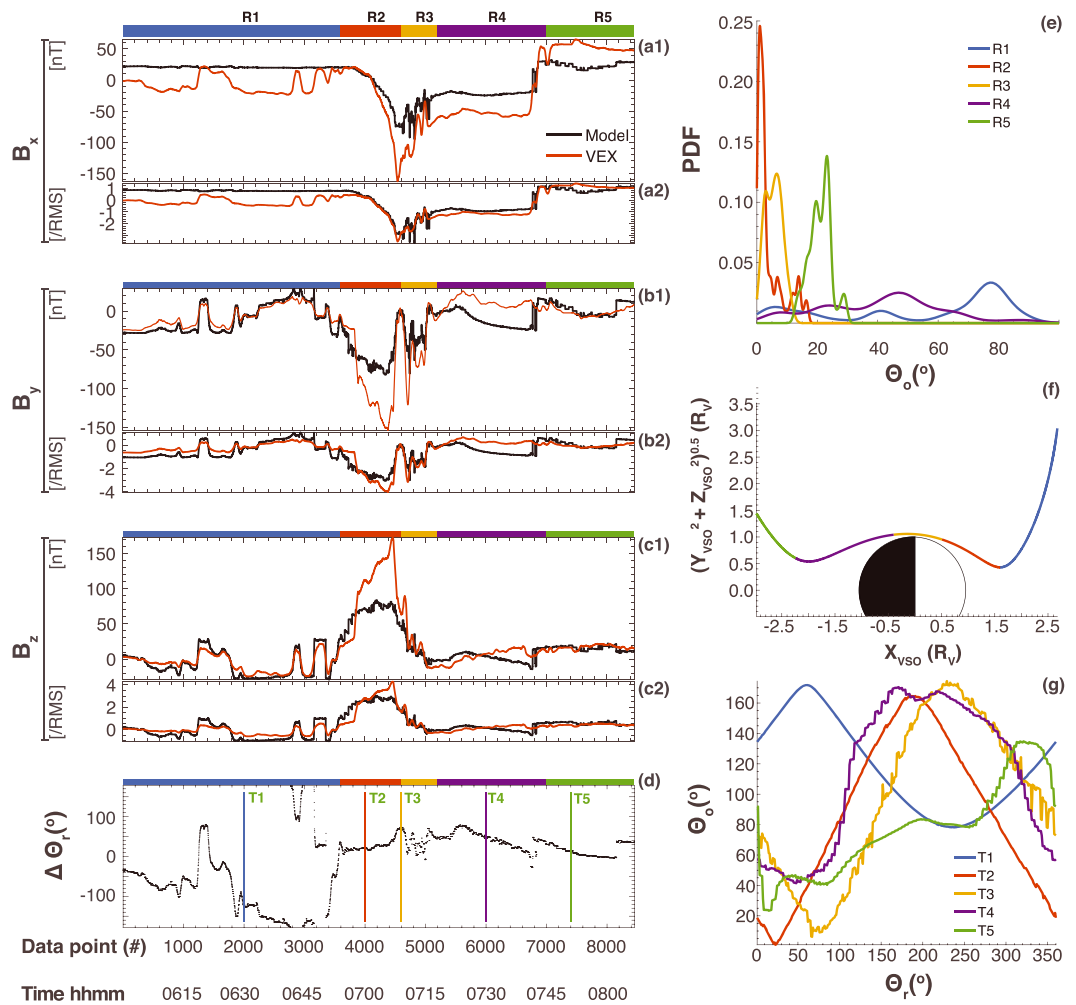


Figure 6. Comparison between the VEX and the hybrid model data during the clock angle optimization procedure for the date 5 November 2011. Panels (a–c) show the VEX-model time series comparison for each magnetic field component. The first subpanels 1 (e.g., a1) indicate the actual field values in nanotesla, whereas subscript 2 refers to the fields normalized by the RMS computed over the entire interval (/RMS). The bottom panel (d) shows the angle of rotation about the x axis required to achieve the optimal angle between the modeled and observed field directions. The five different colors correspond to the following regions (R1–R5): upstream, bow shock to magnetic barrier maximum, periapsis, magnetotail until cross-tail tail current sheet, and magnetotail after cross-tail current sheet. Panel (e) shows PDFs of the angles between the model and VEX field direction for each point after the rotation (i.e., low angles indicate a good agreement). Panel (f) indicates where each region was during the VEX orbit. Panel (g) shows the optimal angle versus the yz plane rotation angle for the times (T1–T5) labeled in panel (d). In effect, panel (g) shows an example of how the optimal angle changes with the rotation angle. It can be seen that in some regions a good optimal angle is achieved (T2), but in other cases a solution was not reached (T5). VEX = Venus Express; RMS = root mean square; PDFs = probability distribution functions.

crossed at approximately 3,400 data points. The interval prior to the bow shock crossing is the ICME sheath region. The optimization procedure is immediately obvious here since the simulated B_x remains almost constant (as the rotation is about the x axis) while the other components track the ICME field rotations relatively accurately. What is clear from Figures 6a1, 6b1, and 6c1 is that the simulation generally underestimates the magnitudes of B_{vex} . Having said that, the normalized components shown in Figures 6a2, 6b2, and 6c2 suggest that the trends of the magnetic field components are well reproduced in the simulated data if the magnitudes of each component are appropriately scaled. Between data points 5,000 and 7,000 (i.e., mostly covering R3 and R4 which covers the periapsis and magnetotail until the cross-tail current sheet), the measured and simulated profiles diverge, and this is particularly visible in the B_y and B_z components shown in Figures 6b and 6c. Note that we suspect, at this point, that the upstream driving has transitioned from ICME sheath ejecta. It should also be stated that the RMS normalization does not correct this; therefore, the magnetic field orienta-

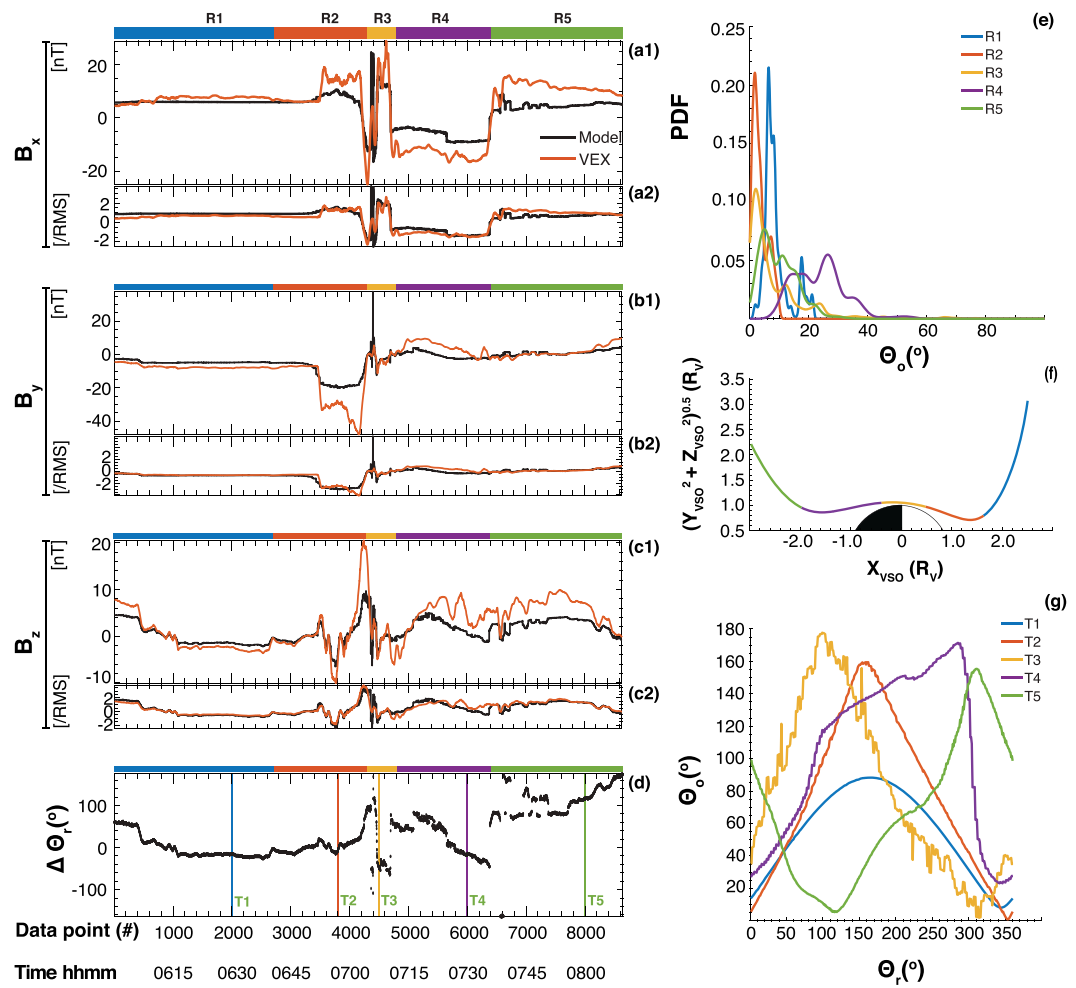


Figure 7. Comparison between the VEX and hybrid model data after the clock angle optimization procedure for a nominal day on 29 October 2011. The format is the same as Figure 6. VEX = Venus Express; PDF = probability distribution function.

tions differ in this region between the measured and simulated data. To quantify the error associated with the optimization, we have plotted the probability distribution functions of Θ_o for five regions labeled R1–R5 in Figure 6e. These regions are marked by the color bars at the top of Figures 6a1, 6b1, 6c1. The orbital location of each region is shown in Figure 6f. In general, region 1 shows a multimodal distribution of error, albeit this is to be expected from the static model input conditions, compared to the dynamic and transient observations. R2, which corresponds to the bow shock crossing and up to the magnetic barrier, shows a high degree of agreement, and the angle is typically between 1° and 5°. R3 covers the trajectory from the magnetic barrier and across the periapsis. Even though the error increases here, Θ_o is typically less than 15°. Moving into the magnetotail (which is R4), the error increases and is spread over 80°, indicative of a poor solution between the observed and modeled field directions. The error appears to decrease for the latter part of the orbit in R5, in which Θ_o is around 20°.

4.2. Optimization for Nominal Day: 29 October 2011

Presented in Figure 7 are the results from simulation-data optimization, except in this case the procedure was performed during a period of nominal solar wind conditions. The format of Figure 7 is the same as in Figure 6. Due to the absence of any clear solar wind structures or significant IMF rotations, the optimization shows good performance in the upstream region (R1) with errors approximately 10°. This is in contrast with the previous interval in which errors over the comparable region were around 80°. It is particularly striking that the dayside errors are comparable between the ambient and extreme periods (see Figures 6g and 7g); this point will be discussed in more detail in the following section. The largest differences between the two

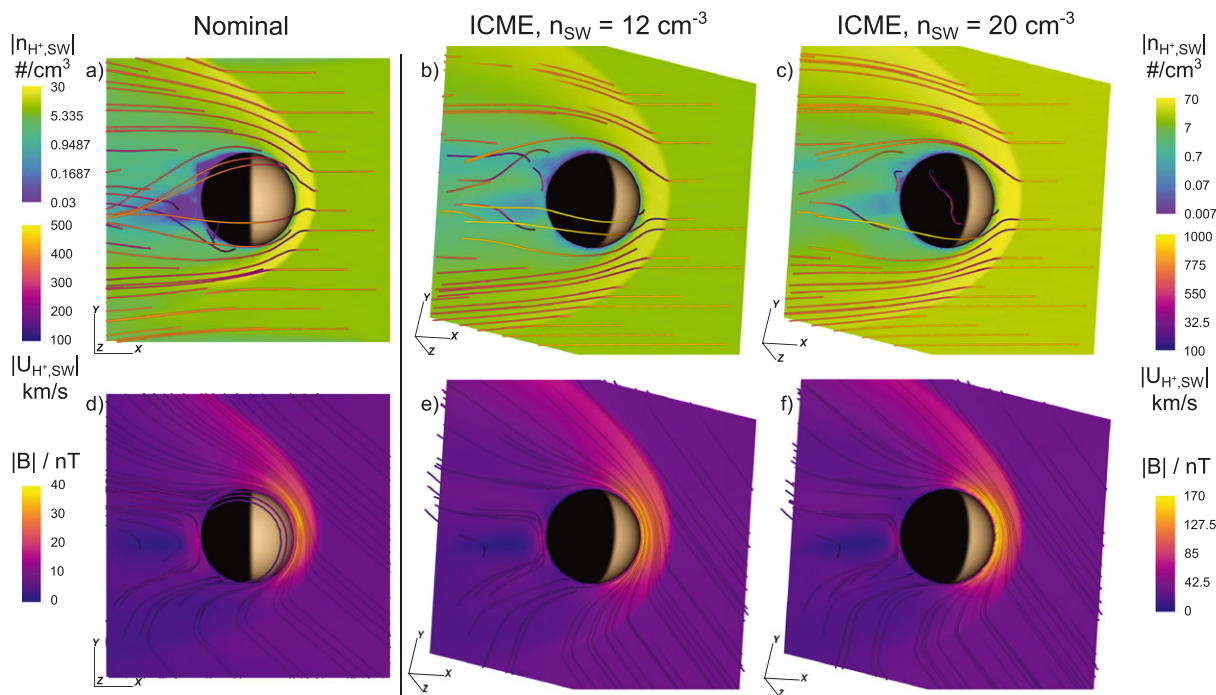


Figure 8. Comparison of the Venus plasma environment for the (a, d) nominal run and the ICME driving conditions (b, c, e, f). The data are presented on a plane spanned by the solar wind velocity and IMF vectors. The color scales for the nominal case are displayed on the left, while the ICME color scales are given on the right. Note that the ICME color scales are identical but different from the nominal. The top row gives the density of solar wind on the slice color and solar wind streamline propagation initiated from the slice plane. The bottom row slice and field line colors give the magnetic field magnitude on the slice and on the field lines connected to the slice. ICME = interplanetary coronal mass ejection; IMF = interplanetary magnetic field.

runs are in the nightside/magnetotail (R4 and R3). In the ICME case, no consistent model-data optimization was possible on the nightside. During the nominal interval, the errors for R4 consistently converged to around 20–30°, and there were negligible errors beyond 40°.

5. Hybrid Simulation Results: Nominal Versus ICME Driving

5.1. Overview

Shown in Figure 8 is a comparison between the n_{20} , n_{12} , and the nominal runs. Each case is a slice from the model result which is taken from the plane that lies perpendicular to the upstream solar wind flow and which contains the undisturbed IMF vectors—the VSO orientation is displayed in the bottom left of each panel. The color in each panel corresponds to the solar wind proton density, whereas the contour lines and color represent the magnetic field magnitude. The streamlines are also included, and their color indicates the speed. What is immediately obvious is that there is a global increase of solar wind proton density during the ICME for both the n_{12} and n_{20} runs. The magnetic field strengths are also enhanced, particularly at the magnetic barrier for the ICME runs compared to nominal conditions. It is also clear that by increasing the upstream number density, the magnetic barrier also increased. Although the general behavior of the model as a function of the strength of the upstream driving conditions is consistent with the observations, the model continually underestimates the magnetic barrier recorded by VEX. Having said that, there does not appear to be a significant impact on the magnetic field draping pattern between the three model runs. In the next section we examine the field line draping properties in more detail.

5.2. Field Line Draping

Presented in Figure 9 is the magnetic field draping during the nominal (left column) and ICME (middle and right columns) runs. The draping is presented in an aberrated frame using the upstream solar wind vector in which the VSO direction is marked next to each panel. Note that in the nominal case, the solar wind flow is approximately parallel to the VSO x axis, and therefore, the VSO and aberrated-nominal frames are quite similar. On the other hand, the aberrated ICME differs to the VSO frame due to the rather oblique upstream flow direction—reflected by the rotated VSO axes. It is worth noting that data which have been rotated

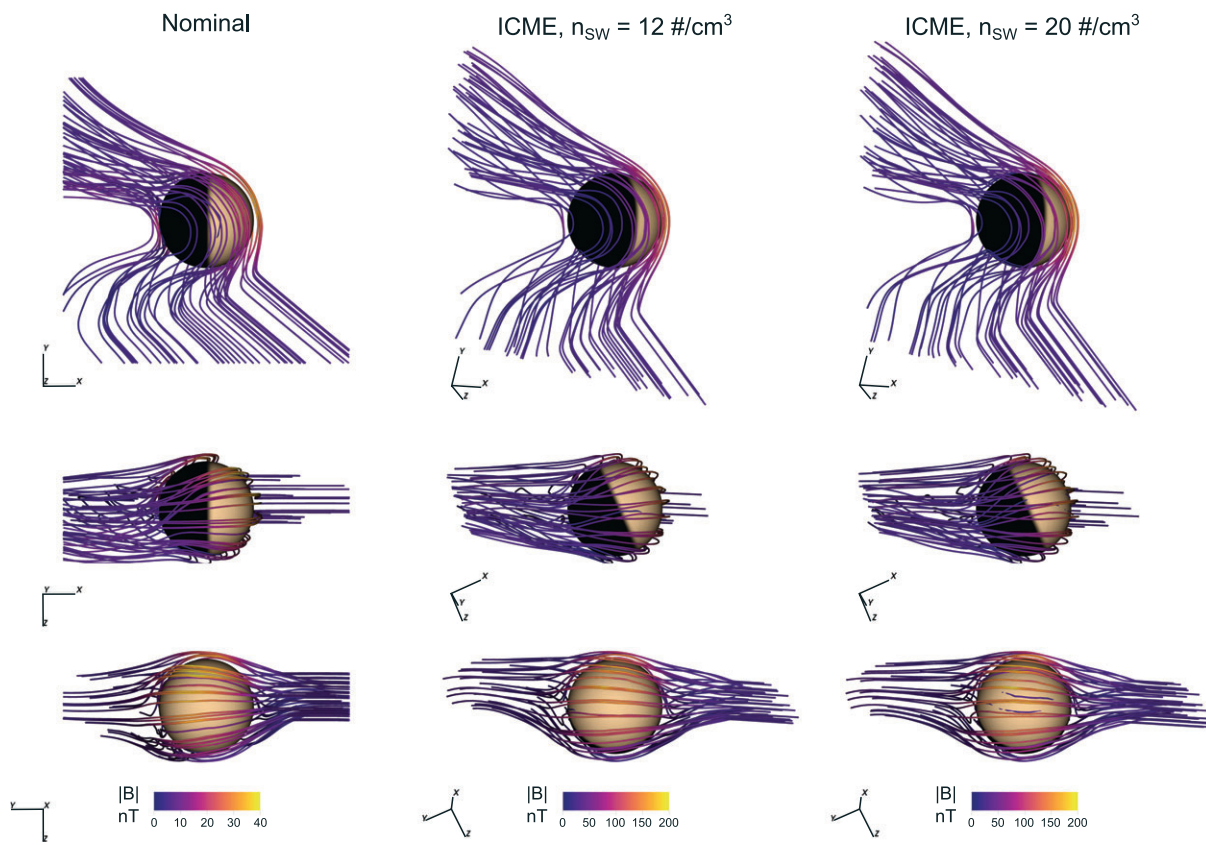


Figure 9. Magnetic field lines and solar wind flow lines for the nominal (left column) and ICME (middle and right columns) conditions. The model data are presented in an aberrated system to reduce asymmetries introduced from oblique solar wind flow. The color on the magnetic field line gives the value of the magnetic field at each position along the line. The color scales for each column are given on the bottom; the scales are identical for the ICME cases and reduced for the nominal case. ICME = interplanetary coronal mass ejection.

(around x), corresponding to the magnetic field vector, also represent conditions where the direction of the transverse velocity component is also rotated about the x axis. Therefore, all rotated simulation cases correspond to cases which had the same upstream U_x and the same magnitude of the total transverse solar wind velocity component $\sqrt{U_y^2 + U_z^2}$ —but the transverse components were rotated by the best fit rotation angle about the x axis. In principle, this causes uncertainty in the optimization procedure since the actual flow orientation is unknown. In practice, the impact from such effects could be estimated by making hundreds of runs for different directions of the transverse velocity component and analyzing model-data discrepancies in detail. However, since we focus on the differences between the magnetic topology, such extensive computations are beyond the scope of this study; but this assumption should be kept in mind.

In both cases, several key regions can easily be identified such as the bow shock, magnetic barrier, and the magnetotail. Interestingly, in both cases, the magnetic field draping patterns are very similar. To put this into context with the model-data comparison, this implies that the large differences between the simulated and observed magnetotail (see Figure 6) are likely induced by variable upstream conditions which the model cannot account for.

From Figure 6 we can see that there is a large deviation between the observations and the model magnetic field directions in R4. In the observations, the magnetic cloud structure can clearly be seen superimposed on the VEX magnetotail, so it is a logical assumption that the upstream driving has changed from the sheath to the ejecta components of the ICME. It is not possible to identify the exact time interval at which the change in the external driving occurred; however, since there is no notable sharp changes in the observations between the bow shock crossing and the magnetic barrier, it is our interpretation that it occurred between R3 and R4 (after the magnetic barrier) which corresponds to an interval from 07:10 to 07:25 on 5 November 2011. The model-data divergence would occur due to the fact that the ICME ejecta significantly alters the magnetic

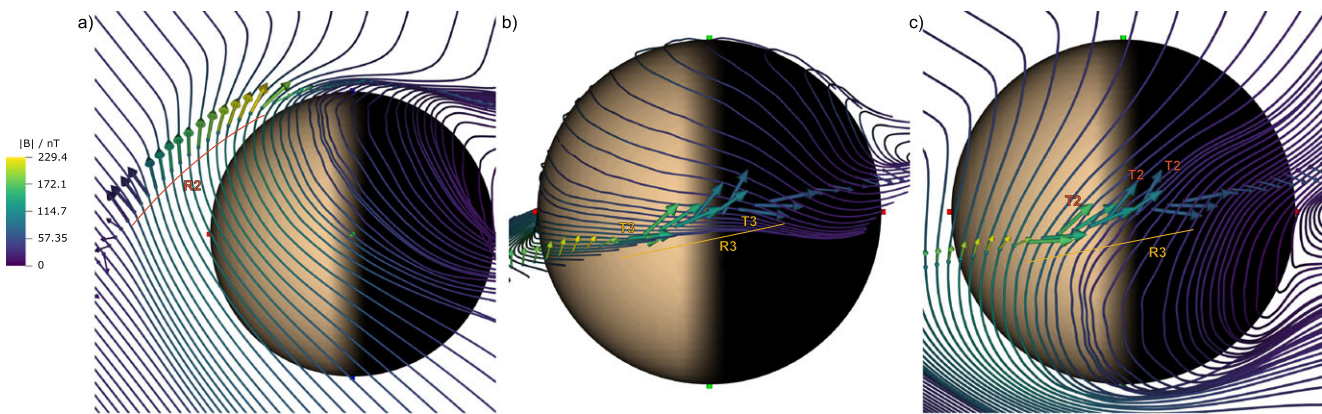


Figure 10. Left to right (R2 at T2, R3 at T3, and R3 at T2) VEX MAG measurements (vectors) and changes in magnetic morphology with respect to clock angle optimizations, as inferred from the simulation (field lines). Please see Figure 6 for descriptions of these regions (R) and times (T). Observations at the region of interest in each subfigure are highlighted with large vector symbols, with the color denoting magnetic field magnitude for both field lines and the observations, at the same scale. The figures illustrate that R3 potentially contains magnetic fields from two separate origins. (a) R2 (including the magnetosheath and the magnetic barrier), with the corresponding rotation of simulated magnetic field. As in Figure 6, the correspondence in magnetic field orientation is good and relatively stable. (b) R3 (postbarrier) magnetic morphology, as given by the clock angle optimization procedure for the corresponding time interval. Points of good magnetic correspondence to the optimized rotation are marked in the figure with T3; the morphology in the simulation at this rotation corresponds to equatorial draping. (c) R3 magnetic morphology, as given by the clock angle optimization to R2 (magnetosheath and barrier), that is, the simulation magnetic field is the same as in the leftmost plot. Points of good correspondence are marked with T2 in the subfigure. The morphology corresponds to draping close to the “pole” of the induced magnetosphere. VEX MAG = Venus Express MAGnetometer.

profile of the magnetotail, which is not included and cannot be accounted for by the model. Thus, in the absence of any variations in the external driving conditions, the draping pattern is similar for the nominal and static modeled ICME driving conditions.

It can be seen in Figure 2 that in the ICME case, the observed magnetic field direction fluctuates below the magnetic barrier in R3. This is also visible in the clock angle optimization procedure in Figure 6d. Taking the optimized clock angles from the procedure for times T2 and T3, we can compare the magnetic morphology of the simulations against the observations, accounting for clock angle dynamics, as demonstrated in Figure 10. In R2, the correspondence is high with the optimized rotation at time T2, but R3 could be seen to be composed roughly of magnetic field perturbations corresponding to rotations at T3 (when entering and leaving R3) and the rotation of the previous region at time T2 (within R3). The differences between the two R3 magnetic field populations are substantial if they are interpreted as clock angle rotations.

Using field rotation at time T3, the morphology corresponds to equator-like draping, while with time T2, the draping corresponds better with the draping pattern close to the nominal pole regions. Notably, the R3 is

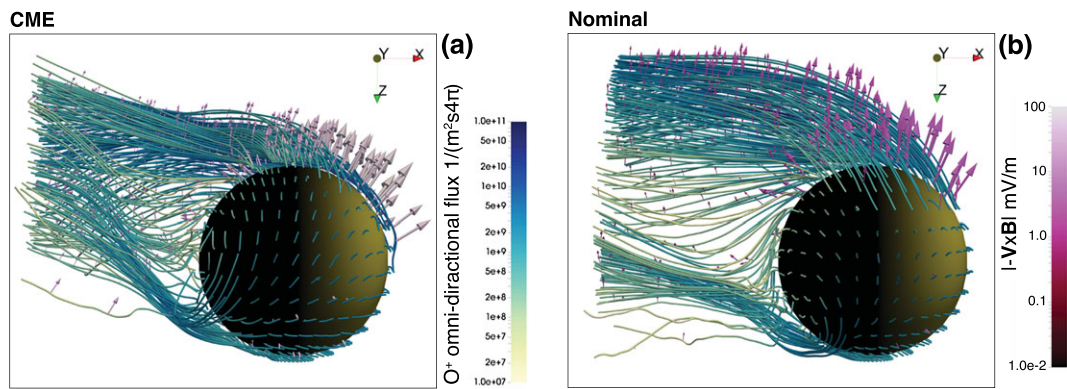


Figure 11. Planetary O⁺ streamlines for (a) ICME and (b) nominal driving conditions. The color of each streamline indicates the omnidirectional flux which was started close to the exobase. Directions of each arrow correspond to the convective electric field, \mathbf{E} , and the color is the magnitude. Note the increase of $|\mathbf{E}|$ for the ICME case, which is reflected by a 30% increase in O⁺ escape. ICME = interplanetary coronal mass ejection.

Table 2*Simulated Total O⁺ Escape Rates (1/s) for the ICME Interval and During Nominal Conditions*

Parameter	Nominal	ICME n_{12}	ICME n_{20}	% change n_{12}	% change n_{20}
Escape rate	2.4809×10^{24}	3.0886×10^{24}	3.2385×10^{24}	+24.5	+30.5
Impact rate	1.1063×10^{25}	1.0601×10^{25}	1.0547×10^{25}	-4.2	-5.03

Note. In all cases, the total O⁺ production rate within the simulation box was fixed as $1.4090 \times 10^{25} \text{ s}^{-1}$. The O⁺ impact rate, that is, the rate of O⁺ ions absorbed at the model exobase, is shown for comparison. The rates are calculated from a 50-s average, after the simulations had reached a quasi-stationary state.

below the magnetic barrier and at low altitudes, hinting to the possibility of remnant solar wind magnetic fields being observed. Indeed, the rough correspondence between a population of observed magnetic fields and field orientation corresponding to previously observed upstream conditions would be consistent with this interpretation.

5.3. Planetary O⁺ and Escape

During the crossing of the magnetotail, the VEX ASPERA-4 instrument detected heavy ions with energies of approximately 10 keV, as seen in Figure 2. These ions were also reported by Vech et al. (2015) to be planetary pickup ions, and we agree with this conclusion. What is noteworthy is that these energies are consistent with the required quantity to achieve O⁺ (Luhmann et al., 2008) escape. Having said that, it is extremely difficult to infer O⁺ escape from such limited spatial coverage—especially since the probe is not located in the mid-to-distant wake, where outward heavy ion trajectories are more reliable evidence (Luhmann et al., 2008). For this reason, we utilize hybrid simulation runs to obtain a more global perspective and convincing evidence of O⁺ escape. In order to test the sensitivity of the O⁺ escape rate on the solar wind density, we made the calculations for both the n_{12} and the n_{20} runs.

Plotted in Figure 11 are the planetary O⁺ streamlines for the ICME n_{20} (a) and nominal (b) runs. The color of each streamline corresponds to the value of the model omnidirectional flux. In both plots, the streamlines are propagated from close to the exobase, which is approximately 200 km. The arrows indicate the directions of the convective ($-\mathbf{U} \times \mathbf{B}$) electric field. It should be noted that the flow lines of the O⁺ ions seen in Figure 11 cannot show in detail how individual planetary O⁺ ions move, since the bulk velocity can include ions which have very different velocities. However, the flow lines illustrate the fact that the O⁺ can be very nongyrotropic because of the large ion gyroradius, compared with the size of the interaction region. In the ICME n_{20} , n_{12} , and nominal cases, there are pickup ions. However, only in the ICME orbit did the VEX spacecraft cross the flow channel and provide evidence (by the ASPERA-4 instrument) of the presence of energetic heavy ions. This is also demonstrated by the VEX observations in Figures 1 and 2 in which energized O⁺ ions are recorded by ASPERA-4 (around 10 keV). As expected, the convective electric field increases during the ICME driving conditions (n_{20}) shown in Figure 11a. This is also reflected by increased O⁺ escape during the ICME. The escape rates for both cases are summarized in Table 2. The escape rates are computed from the number of ions which are escaping from the simulation box. It is important to note that in both cases, the quantity of O⁺ production is the same since both possess the same ionosphere and exobase. Thus, the distribution of the newly formed planetary ions is identical. As already mentioned, the Venus ionosphere is treated as a fully conducting obstacle, at a fixed height, so hysteresis effects are excluded, and possible effects of the ICME on the ionosphere are also neglected. As a result, the differences in escape rates are purely a consequence of the upstream conditions and thus the ICME driving. From the values in Table 2, we estimate that during the ICME driving interval, there is approximately a 30% increase in O⁺ escape for the n_{20} run and 24.5% for the n_{12} run. The ICME rates are computed relative to the nominal run.

6. Discussion

In this work, we have analyzed the Venus IM during an ICME using observations from VEX and hybrid simulations. We compared the observed and simulated draping patterns as a metric to determine the feasibility of modeling the Venus solar wind interaction during ICME sheath conditions. The model results were then used to determine the escape of planetary heavy ions (O⁺) resulting from the enhanced solar wind convective electric field. We also investigated the factors leading to an extraordinary 250-nT magnetic barrier encounter. We

briefly employed 32-Hz VEX MAG measurements to report the presence of substantial electromagnetic wave activity spanning the interval from upstream of the bow shock through to the downstream magnetosheath.

Arguably, the most striking observation on 5 November 2011 was the extremely larger magnetic barrier which exceeded 250 nT, as shown in Figures 1 and 2. In Figure 4 we plotted the normalized magnetic field profile from upstream to after the magnetic barrier into the nightside. From our analysis, there is not one clear mechanism which would drive such an atypically large magnetic barrier. However, there are several distinct factors which may contribute and eventually go to great lengths to explain this. First, the compression ratio of the shock is larger, which results in an increased downstream magnetic field strength. Second, the dayside appears to be unusually compressed, which is evidenced by the short traversal of the magnetosheath by VEX, and this is consistent with the large positive gradient of the magnetic field from downstream to the magnetic barrier. Third, the upstream conditions already consist of “shocked” plasma from the ICME sheath which is heated, dense, and contains a large magnetic field strength (determined from ASPERA-4 energy spectra). This combination of plasma parameters provides substantial external pressure driving which is physically consistent with the above interpretations. We must also take into account the duration of the ICME sheath driving, since VEX crosses the bow shock after the ICME sheath has been present for several hours. This prolonged external driving allows magnetic flux to pileup against the magnetic barrier obstacle for considerable time, which likely plays a role.

It is also noteworthy that the magnetic profile after the magnetic barrier is markedly different during the ICME passage. Our interpretation of this is that due to the larger external pressure from the ICME, the ionosphere becomes magnetized. A magnetized ionosphere occurs if the pressure balance is achieved in the collisional region (a few hundred kilometers) due to high external pressure driving—as is the case here. In these circumstances, the magnetic field does not drop as sharply as the unmagnetized case and instead diffuses and convects downward toward the ionosphere (see Futaana et al., 2017, and references therein). Measurements of comparable magnitude magnetic barriers are extremely rare, and to our knowledge, this is the largest that VEX recorded. We believe that an explanation for such a rare observation is that (like this example) there are numerous physical and technical criteria which have to be met in order for such an event to be recorded. Out of these criteria, a period of prolonged external pressure driving and magnetic flux pileup is arguably the most important. In terms of the model results, it is important to note that the magnetic barrier was always underestimated (compared to VEX) by the model. Between the n_{12} and n_{20} runs, the modeled barrier strength did increase, which is consistent with the hypothesis above in the sense that large external pressure contributions played a strong role in the 250-nT barrier observation. We should also mention that the lack of a self-consistent ionosphere may play a role, and therefore, this topic may be revised later when a more sophisticated treatment of the ionosphere and time-dependent input capabilities is added to the model.

During the model-data comparison presented in Figures 6 and 7, the procedure reached an optimal solution for the entire VEX orbit during nominal conditions, suggesting that the model can reproduce an accurate global draping pattern. On the contrary, during the ICME n_{20} run, the procedure converged on the dayside but failed to do so on the nightside; the result was also the same for the n_{12} run. There are several explanations for this. First, taking into consideration the modeled draping pattern, discrepancies may be introduced partly due to the model, which does not have a self-consistent ionosphere, along with a relatively coarse spatial resolution. Second, any inaccuracies in the measured upstream conditions would play a significant role, particularly the plasma measurements, which are crucial to implementing a comparable model run. The density measured inside ICME sheath regions can vary significantly, with peaks up to $30\text{--}60\text{ cm}^{-3}$ observed (Das et al., 2011); the highest densities in ICME sheaths are often found close to the shock and ejecta and are termed pileup compression regions (PUC; Das et al., 2011). Therefore, the occurrence of such high-density structures could lead to the enhanced magnetic barrier and differences in the model-data comparison. This was also a motivation for making the two ICME runs with varying density. Finally, the divergence of the measured magnetotail is likely due to the ICME ejecta, which is visible in the magnetotail profile (also reported by Vech et al., 2015). However, according to Figure 9, and based entirely on the ICME sheath input parameters, the simulated magnetic configuration of the magnetotail did not appear significantly altered compared to the nominal run. It should also be noted that in a run where the solar wind flow is not exactly along the model x axis, the rotation procedure also rotates the solar wind velocity vector. Therefore, the rotated solutions cannot exactly describe similar solar wind flow situations for different IMF conditions. In the ICME case, the upstream flow direction is approximately 23.7° with respect to the VSO x axis during the ICME sheath—any differences introduced from this small oblique flow are excluded from these results.

Previous studies (e.g., Luhmann et al., 2008, and references therein) which investigate the simulated Venus-ICME interaction have typically focused on the ICME ejecta component, since the evolution of the field and plasma properties occur much slower compared to the sheath region. However, based on the good model-data solution on the dayside (until the ICME ejecta), we conclude that it is also feasible to model the ICME sheath conditions. Nevertheless, once a transition from the ICME sheath to the ejecta occurs (see Figure 1b between 32 and 35 hr), any model-data comparisons from that point are likely to diverge. We suspect that this was the reason for the divergence between the model-data solution observed in R4 in Figure 6. For that reason, it is challenging to infer global conclusions from ICME sheath and ejecta of the same event. We suggest that the best approach for such studies should be statistical that focus on individual regions separately. Another option is to utilize models which can handle upstream transients, and this may be revisited as the hybrid model is developed further.

The atypically high dynamic pressures of ICME events have many effects, namely, magnetizing the ionosphere and reducing the altitude of the ionopause (Luhmann & Cravens, 1991). In some circumstances, these can potentially increase the number of planetary ions which are lost. We investigated this by computing the O⁺ escape rates for each of our runs. These calculations resulted in 30.5% and 24.5% increases (with respect to the nominal run) of O⁺ escape for the n_{20} and n_{12} ICME sheath runs, respectively. In a similar study, Luhmann et al. (2008) concluded that from four examined ICMEs, in only one case could they report increases in O⁺ escape flux. However, it is important to keep in mind that their cases were ICME ejecta driven, which typically have lower densities compared to our ICME sheath case. We investigated the role of density in Table 2, which showed elevated O⁺ for a larger upstream density. This conclusion is consistent with that of Liu et al. (2009) who reported a similar relationship. These results are indicative of variable O⁺ escape rates for sheath and ejecta conditions in which the value is larger for the sheath region. A likely cause of this is the generally higher densities during the ICME sheaths. On the other hand, these regions present more challenging conditions from a modeling standpoint. We should also reiterate that the ionosphere is kept constant between each run, meaning that any impact of the ICME on the ionosphere is neglected. For that reason, any quoted escape rates are purely a response from upstream conditions. In addition, Liu et al. (2009) reported that “the IMF x component enhances the O⁺ escape rate.” This is important to note, as our model did not include upstream transients and indeed cannot introduce transients in the IMF B_x component. Therefore, any effects from transient IMF B_x behavior are excluded from these results. It would be a worthwhile endeavor for future investigators who have the capability to introduce transient upstream conditions to quantify this effect in more detail.

Finally, the 32-Hz resolution VEX MAG data exhibited clear wave activity upstream and downstream of the bow shock front. Based on our analysis, we concluded that these upstream fluctuations are likely dispersive whistler precursors associated with the bow shock which help to balance the shock front steepening (Kennel et al., 1985). Very similar 1-Hz waves were reported by Orlowski and Russell (1991) in the Venus foreshock who also suggested that they could be whistler mode waves generated at the bow shock. This generation mechanism and wave properties are comparable to numerous observations upstream of the terrestrial bow shock (Fairfield, 1974) and other planetary bow shocks (Russell, 2007). It is also worth mentioning that ion cyclotron waves were observed upstream of the bow shock by Delva et al. (2008). However, the wave properties we observe are more consistent with the whistler mode. Regarding the downstream waves, these contained relatively large amplitudes ($|\mathbf{B}_{\text{RMS}}|/\langle|\mathbf{B}|\rangle \sim 20\%$). Their period is approximately 1 s, placing them slightly below the local ion gyrofrequency. A possible candidate for these is ion-cyclotron waves which can be generated by the ion pickup process (Russell et al., 2006). However, since we were unable to determine the expected parallel propagation, we conclude that these may be whistler waves originating upstream. This is supported by the similar polarization (see Figure 5) and propagation angle. It is also worth noting that whistler waves were observed until the shock ramp and inside the foot region which exhibited extremely similar characteristics (not shown). We should also mention that Venus magnetosheath turbulence has been attributed to the bow shock itself. We ruled these out since these variations were associated with a quasi-parallel bow shock and possess periods of 10–40 s (Du et al., 2009; Luhmann et al., 1983), which are significantly below what we observed. It is difficult to determine the role of the observed waves in the ICME-Venus interaction, for which more work and event studies are required. Nevertheless, their occurrence is worth reporting, as it clearly demonstrates that future investigators should also consider small-scale structures close to and above the local gyrofrequency when studying similar events. In addition, to describe these complex nonlinear effects, models will need the appropriate resolution in order to resolve ion-scale effects.

7. Summary and Conclusions

We can summarize the main results of this study as follows:

1. We have studied the properties and the response of the Venus IM in the extreme case when the planet was embedded inside an ICME and when atypically high magnetic field values (~ 250 nT) were observed.
2. Numerous factors may have resulted in an extremely large magnetic barrier, and the prolonged external pressure driving and magnetic flux pileup seem likely to play a dominant role.
3. During the ICME passage, VEX MAG data suggested that the ionosphere became magnetized, and the bow shock moved closer to the planet whereas the effect on the magnetic barrier location was negligible.
4. Global large-scale analysis based on 3-D hybrid model simulations suggest that the magnetic field draping pattern during the ICME sheath passage was much alike during the nominal solar wind conditions. The simulation was found to reproduce the magnetic field draping pattern on the dayside relative well but poorly on the nightside. This is likely the result of the upstream conditions changing from the sheath to ejecta. Moreover, upstream ICME sheath conditions resulted in around a 30% increase in the total O^+ escape rate.
5. This study has demonstrated that hybrid simulation runs are also applicable to extreme ICME cases, even when the upstream conditions are highly dynamic. Having said that, one has to err on the side of caution, as model-data solutions diverge once the ICME state changes.
6. The analysis of the small spatial scale and fast phenomena made by high-resolution magnetic field observations showed that during the ICME passage, large-amplitude upstream and downstream waves were observed. The waves cannot be characterized unambiguously but are likely to be whistler waves convected from upstream to downstream.

To conclude, both experimental data and hybrid numerical simulations have demonstrated that the Venusian plasma environment can be significantly altered during extreme driving events such as ICMEs. However, to fully understand the extent of these interactions, both data and numerical models are required to infer global effects such as O^+ escape rates. This work has shed some light on various aspects of these interactions, and also, open questions remain. While our results suggest that the O^+ escape rates are elevated for ICME sheath conditions, it is still unclear if similar escape rates can be quoted for the ICME ejecta part. This will likely require future studies using many events and utilizing numerical models. Fortunately, the extensive VEX catalog contains many ICME-Venus encounters. Another important aspect is the presence, and role of electromagnetic waves during Venus-ICME interactions, whose roles are not fully understood. A large-scale statistical study of their properties and potential consequences is also warranted. One main point to take away from this work is that it is indeed feasible to model the dynamic ICME sheath intervals, but one should carefully consider the upstream time-dependant conditions since model-data comparisons diverge once the upstream conditions switch to the ICME ejecta. Understanding the conditions and physical mechanisms which result in large magnetic barriers is also important, and a follow-up study on many more (albeit less extreme) events, is justified. In addition, these results are also applicable and of interest to other planetary bodies. Although other planets differ in terms of composition, intrinsic magnetic field, and chemistry, they often contain surprisingly similar regions and boundaries which are heavily affected by ICME passages. Finally, with increasing complexity and performance of numerical models, future studies should focus on modeling such interactions in greater detail by including turbulence and variation of plasma and field properties intrinsic to ICME sheaths, with a more sophisticated treatment of the ionosphere, which evidently is affected.

References

Ayachit, U. (2015). *The ParaView guide: A parallel visualization application*. USA: Kitware, Inc.

Balikhin, M. A., Zhang, T. L., Gedalin, M., Ganushkina, N. Y., & Pope, S. A. (2008). Venus express observes a new type of shock with pure kinematic relaxation. *Geophysical Research Letters*, 35, L01103. <https://doi.org/10.1029/2007GL032495>

Barabash, S., Fedorov, A., Sauvaud, J. J., Lundin, R., Russell, C. T., Futaana, Y., et al. (2007). The loss of ions from Venus through the plasma wake. *Nature*, 450, 650–653. <https://doi.org/10.1038/nature06434>

Barabash, S., Sauvaud, J.-A., Gunell, H., Andersson, H., Grigoriev, A., Brinkfeldt, K., et al. (2007). The analyser of space plasmas and energetic atoms (ASPERA-4) for the Venus express mission. *Planetary and Space Science*, 55, 1772–1792. <https://doi.org/10.1016/j.pss.2007.01.014>

Burlaga, L., Sittler, E., Mariani, F., & Schwenn, R. (1981). Magnetic loop behind an interplanetary shock: Voyager, Helios, and IMP 8 observations. *Journal of Geophysical Research*, 86(A8), 6673–6684. <https://doi.org/10.1029/JA086iA08p06673>

Childs, H., Brugger, E., Whitlock, B., Meredith, J., Ahern, S., Pugmire, D., et al. (2012). VisIt: An end-user tool for visualizing and analyzing very large data. In *High performance visualization—Enabling extreme-scale scientific insight* (pp. 357–372). Hoboken: CRC.

Coates, A. J., Fahrm, R. A., Linder, D. R., Kataria, D. O., Soobiah, Y., Collinson, G., et al. (2008). Ionospheric photoelectrons at Venus: Initial observations by ASPERA-4 ELS. *Planetary and Space Science*, 56, 802–806. <https://doi.org/10.1016/j.pss.2007.12.008>

Acknowledgments

We would like to acknowledge the efforts made by the entire Venus Express team, most of all, the members of the magnetometer and ASPERA-4 teams. Thanks to C. S. Wedlund for comments relating to the hybrid model configuration and A. Osmane for discussions of magnetosheath turbulence. Special thanks to M. Delva for consultation regarding the 32-Hz data and observed wave modes. A. P. Dimmock and T. I. Pulkkinen would like to acknowledge financial support from the Academy of Finland grants 288472, 267073/2013, and 310444. A. J. C. acknowledges support from the STFC consolidated grant to UCL-MSSL. The Venus Express data are openly available at the European Space Agency's Planetary Science Archive ([www.rssd.esa.int/PSA](http://rssd.esa.int/PSA)) and the AMDA (<http://amda.cdpp.eu/>) science analysis system provided by the Centre de Données de la Physique des Plasmas (IRAP, Université Paul Sabatier, Toulouse) supported by CNRS and CNES. The open source visualization software VisIt (Childs et al., 2012) and ParaView (Ayachit, 2015) were used to produce some of the figures. VisIt is supported by the Department of Energy with funding from the Advanced Simulation and Computing Program and the Scientific Discovery through Advanced Computing Program.

Das, I., Opher, M., Evans, R., Loesch, C., & Gombosi, T. I. (2011). Evolution of piled-up compressions in modeled coronal mass ejection sheaths and the resulting sheath structures. *The Astrophysical Journal*, 729, 112. <https://doi.org/10.1088/0004-637X/729/2/112>

Delva, M., Zhang, T. L., Volwerk, M., Magnes, W., Russell, C. T., & Wei, H. Y. (2008). First upstream proton cyclotron wave observations at Venus. *Geophysical Research Letters*, 35, L03105. <https://doi.org/10.1029/2007GL032594>

Dimmock, A. P., Balikhin, M. A., Walker, S. N., & Pope, S. A. (2013). Dispersion of low frequency plasma waves upstream of the quasi-perpendicular terrestrial bow shock. *Annales Geophysicae*, 31, 1387–1395. <https://doi.org/10.5194/angeo-31-1387-2013>

Du, J., Zhang, T. L., Wang, C., Volwerk, M., Delva, M., & Baumjohann, W. (2009). Magnetosheath fluctuations at Venus for two extreme orientations of the interplanetary magnetic field. *Geophysical Research Letters*, 36, L09102. <https://doi.org/10.1029/2009GL037725>

Edberg, N. J. T., Nilsson, H., Futaana, Y., Stenberg, G., Lester, M., Cowley, S. W. H., et al. (2011). Atmospheric erosion of Venus during stormy space weather. *Journal of Geophysical Research*, 116, A09308. <https://doi.org/10.1029/2011JA016749>

Fairfield, D. H. (1974). Whistler waves observed upstream from collisionless shocks. *Journal of Geophysical Research*, 79, 1368–1378. <https://doi.org/10.1029/JA079i010p01368>

Futaana, Y., Stenberg Wieser, G., Barabash, S., & Luhmann, J. G. (2017). Solar wind interaction and impact on the Venus atmosphere. *Space Science Reviews*, 212(3), 1453–1509. <https://doi.org/10.1007/s11214-017-0362-8>

Jarvinen, R., Kallio, E., & Dyadechkin, S. (2013). Hemispheric asymmetries of the Venus plasma environment. *Journal of Geophysical Research: Space Physics*, 118, 4551–4563. <https://doi.org/10.1002/jgra.50387>

Jarvinen, R., Kallio, E., Janhunen, P., Barabash, S., Zhang, T. L., Pohjola, V., & Sillanpää, I. (2009). Oxygen ion escape from Venus in a global hybrid simulation: Role of the ionospheric O⁺ ions. *Annales Geophysicae*, 27, 4333–4348. <https://doi.org/10.5194/angeo-27-4333-2009>

Kallio, E. (2005). Formation of the lunar wake in quasi-neutral hybrid model. *Geophysical Research Letters*, 32, L06107. <https://doi.org/10.1029/2004GL021989>

Kallio, E., Fedorov, A., Budnik, E., Säles, T., Janhunen, P., Schmidt, W., et al. (2006). Ion escape at Mars: Comparison of a 3-D hybrid simulation with Mars Express IMA/ASPERA-3 measurements. *Icarus*, 182, 350–359. <https://doi.org/10.1016/j.icarus.2005.09.018>

Kallio, E., & Janhunen, P. (2003). Modelling the solar wind interaction with Mercury by a quasi-neutral hybrid model. *Annales Geophysicae*, 21, 2133–2145. <https://doi.org/10.5194/angeo-21-2133-2003>

Kallio, E., Jarvinen, R., & Janhunen, P. (2006). Venus solar wind interaction: Asymmetries and the escape of O⁺ ions. *Planetary and Space Science*, 54(13), 1472–1481. <https://doi.org/10.1016/j.pss.2006.04.030>, The Planet Venus and the Venus Express Mission.

Kallio, E., Zhang, T. L., Barabash, S., Jarvinen, R., Sillanpää, I., Janhunen, P., et al. (2008). The Venusian induced magnetosphere: A case study of plasma and magnetic field measurements on the Venus Express mission. *Planetary and Space Science*, 56, 796–801. <https://doi.org/10.1016/j.pss.2007.09.011>

Kennel, C. F., Edmiston, J. P., & Hada, T. (1985). A quarter century of collisionless shock research. In R. G. Stone & B. T. Tsurutani (Eds.), *Collisionless shocks in the heliosphere: A tutorial review* (Vol. 34, pp. 1–36). Washington, DC: American Geophysical Union.

Kilpua, E. K. J., Isavnin, A., Vourlidas, A., Koskinen, H. E. J., & Rodriguez, L. (2013). On the relationship between interplanetary coronal mass ejections and magnetic clouds. *Annales Geophysicae*, 31(7), 1251–1265. <https://doi.org/10.5194/angeo-31-1251-2013>

Leinweber, H. K., Russell, C. T., Torkar, K., Zhang, T. L., & Angelopoulos, V. (2008). An advanced approach to finding magnetometer zero levels in the interplanetary magnetic field. *Measurement Science and Technology*, 19(5), 55104. <https://doi.org/10.1088/0957-0233/19/5/055104>

Liu, K., Kallio, E., Jarvinen, R., Lammer, H., Lichtenegger, H., Kulikov, Y., et al. (2009). Hybrid simulations of the O⁺ ion escape from Venus: Influence of the solar wind density and the IMF x component. *Advances in Space Research*, 43(9), 1436–1441. <https://doi.org/10.1016/j.asr.2009.01.005>

Luhmann, J., Ledvina, S., Lyon, J., & Russell, C. (2006). Venus O⁺ pickup ions: Collected PVO results and expectations for Venus Express. *Planetary and Space Science*, 54(13), 1457–1471. <https://doi.org/10.1016/j.pss.2005.10.009>

Luhmann, J. G., & Cravens, T. E. (1991). Magnetic fields in the ionosphere of Venus. *Space Science Reviews*, 55, 201–274. <https://doi.org/10.1007/BF00177138>

Luhmann, J. G., Fedorov, A., Barabash, S., Carlsson, E., Futaana, Y., Zhang, T. L., et al. (2008). Venus express observations of atmospheric oxygen escape during the passage of several coronal mass ejections. *Journal of Geophysical Research*, 113, E00B04. <https://doi.org/10.1029/2008JE003092>

Luhmann, J. G., Kasprzak, W. T., & Russell, C. T. (2007). Space weather at Venus and its potential consequences for atmosphere evolution. *Journal of Geophysical Research*, 112, E04510. <https://doi.org/10.1029/2006JE002820>

Luhmann, J. G., & Kozyra, J. U. (1991). Dayside pickup oxygen ion precipitation at Venus and Mars—Spatial distributions, energy deposition and consequences. *Journal of Geophysical Research*, 96, 5457–5467. <https://doi.org/10.1029/90JA01753>

Luhmann, J. G., Tatryllyay, M., Russell, C. T., & Winterhalter, D. (1983). Magnetic field fluctuations in the Venus magnetosheath. *Geophysical Research Letters*, 10(8), 655–658. <https://doi.org/10.1029/GL010i008p00655>

Mihalov, J. D., & Barnes, A. (1982). The distant interplanetary wake of Venus—Plasma observations from Pioneer Venus. *Journal of Geophysical Research*, 87, 9045–9053. <https://doi.org/10.1029/JA087iA11p09045>

Moore, K. R., McComas, D. J., Russell, C. T., Shahara, S. S., & Spreiter, J. R. (1991). Gasdynamic modeling of the Venus magnetotail. *Journal of Geophysical Research*, 96, 5667–5681. <https://doi.org/10.1029/90JA02251>

Orlowski, D. S., & Russell, C. T. (1991). Ulf waves upstream of the Venus bow shock: Properties of one-hertz waves. *Journal of Geophysical Research*, 96(A7), 11,271–11,282. <https://doi.org/10.1029/91JA01103>

Phillips, J. L., & Russell, C. T. (1987). Upper limit on the intrinsic magnetic field of Venus. *Journal of Geophysical Research*, 92, 2253–2263. <https://doi.org/10.1029/JA092iA03p02253>

Pope, S. A., Zhang, T. L., Balikhin, M. A., Delva, M., Hvzdos, L., Kudela, K., & Dimmock, A. P. (2011). Exploring planetary magnetic environments using magnetically unclean spacecraft: A systems approach to VEX MAG data analysis. *Annales Geophysicae*, 29(4), 639–647. <https://doi.org/10.5194/angeo-29-639-2011>

Russell, C. (2007). Upstream whistler-mode waves at planetary bow shocks: A brief review. *Journal of Atmospheric and Solar-Terrestrial Physics*, 69, 1739–1746. <https://doi.org/10.1016/j.jastp.2006.11.004>

Russell, C., Mayerberger, S., & Blanco-Cano, X. (2006). Proton cyclotron waves at Mars and Venus. *Advances in Space Research*, 38(4), 745–751. <https://doi.org/10.1016/j.asr.2005.02.091>, Mercury, Mars and Saturn.

Russell, C. T. (1991). *Venus aeronomy*. Dordrecht: Kluwer Academic.

Russell, C. T., Elphic, R. C., & Slavin, J. A. (1979). Initial pioneer Venus magnetic field results—Dayside observations. *Science*, 203, 745–748. <https://doi.org/10.1126/science.203.4382.745>

Russell, C. T., & Zhang, T.-L. (1992). Unusually distant bow shock encounters at Venus. *Geophysical Research Letters*, 19(8), 833–836. <https://doi.org/10.1029/92GL00634>

Svedhem, H., Titov, D. V., McCoy, D., Lebreton, J.-P., Barabash, S., Bertaux, J.-L., et al. (2007). Venus Express—The first European mission to Venus. *Planetary and Space Science*, 55, 1636–1652. <https://doi.org/10.1016/j.pss.2007.01.013>

Vech, D., Szego, K., Opitz, A., Kajdic, P., Fraenz, M., Kallio, E., & Alho, M. (2015). Space weather effects on the bow shock, the magnetic barrier, and the ion composition boundary at Venus. *Journal of Geophysical Research: Space Physics*, 120, 4613–4627. <https://doi.org/10.1002/2014JA020782>

Walker, S. N., Balikhin, M. A., Zhang, T. L., Gedalin, M. E., Pope, S. A., Dimmock, A. P., & Fedorov, A. O. (2011). Unusual nonlinear waves in the Venusian magnetosheath. *Journal of Geophysical Research*, 116, A01215. <https://doi.org/10.1029/2010JA015916>

Wei, H. Y., Russell, C. T., Zhang, T. L., & Blanco-Cano, X. (2011). Comparative study of ion cyclotron waves at Mars, Venus and Earth. *Planetary and Space Science*, 59, 1039–1047. <https://doi.org/10.1016/j.pss.2010.01.004>

Wood, B. E., Müller, H.-R., Zank, G. P., Linsky, J. L., & Redfield, S. (2005). New mass-loss measurements from astrospheric Ly α absorption. *The Astrophysical Journal Letters*, 628, L143–L146. <https://doi.org/10.1086/432716>

Zhang, T. L., Baumjohann, W., Delva, M., Auster, H.-U., Balogh, A., Russell, C. T., et al. (2006). Magnetic field investigation of the Venus plasma environment: Expected new results from Venus Express. *Planetary and Space Science*, 54, 1336–1343. <https://doi.org/10.1016/j.pss.2006.04.018>

Zhang, T. L., Delva, M., Baumjohann, W., Auster, H.-U., Carr, C., Russell, C. T., et al. (2007). Little or no solar wind enters Venus' atmosphere at solar minimum. *Nature*, 450, 654–656. <https://doi.org/10.1038/nature06026>

Zhang, T. L., Delva, M., Baumjohann, W., Volwerk, M., Russell, C. T., Barabash, S., et al. (2008). Initial Venus Express magnetic field observations of the Venus bow shock location at solar minimum. *Planetary and Space Science*, 56, 785–789. <https://doi.org/10.1016/j.pss.2007.09.012>

Zhang, T. L., Luhmann, J. G., & Russell, C. T. (1991). The magnetic barrier at Venus. *Journal of Geophysical Research*, 96(A7), 11,145–11,153. <https://doi.org/10.1029/91JA00088>

Zhang, T. L., Pope, S., Balikhin, M., Russell, C. T., Jian, L. K., Volwerk, M., et al. (2008). Venus Express observations of an atypically distant bow shock during the passage of an interplanetary coronal mass ejection. *Journal of Geophysical Research*, 113, E00B12. <https://doi.org/10.1029/2008JE003128>